NTNU

Norwegian University of
Science and Technology

Fundamental Theories and Methodologies for Assessing Radiation Hardness in Hydrogen-Terminated Diamond

Vilde Flognfeldt Rieker

Master of Science in Physics and Mathematics
Submission date: July 2018
Supervisor: Justin Wells, IFY

Norwegian University of Science and Technology
Department of Physics

FUNDAMENTAL THEORIES AND METHODOLOGIES FOR ASSESSING RADIATION HARDNESS IN HYDROGEN-TERMINATED DIAMOND

TFY4900 Physics Master's Thesis

Vilde Flognfeldt Rieker

July 2018

Abstract

The harsh radiation environment in Space is a challenge for the viability and reliability of electronics aboard spacecrafts. The van Allen radiation belts constitute highly energetic electrons and protons trapped by the magnetic field surrounding Earth. To ensure operability of a satellite, the solution has traditionally been to use space qualified electronics. However, space qualification involves radiation hardening and testing of electronic components, which is an expensive and time-consuming process. This leads to costly and in time obsolete technology that is incompatible with an increasingly commercialized space industry. The demand for more easily accessible and cheaper state-of-the-art components encourages development of devices with inherent radiation hardened properties.

Diamond is a physically hard material which has both high thermal conductivity and breakdown field. This means that they can sustain high power and operate in environments of extreme temperatures and radiation. For this reason, diamond based semiconductors seems promising as substitute for traditional semiconductor materials for electronic devices in future space missions. This thesis focuses on investigating the different effects that may be caused by radiation in diamond with the aim of creating a better foundation to determine whether or not diamond is superior to common semiconductor materials for space electronics.

The origin of conductivity in hydrogen terminated diamond, and the effect of MoO_3 deposition is explained. Further, the various effects that can be induced upon particle irradiation and the mechanisms behind them is elaborated. MoO_3 was deposited on two diamond Hall bar samples, which was then exposed to 3.5 keV electrons and 5 keV helium ions. The *I-V* characterization before and after exposure showed a decrease in conductivity in both cases, which was most likely caused by desorption of hydrogen. However one of the devices that was exposed to helium ions attained a strong increase in conductivity. Raman analysis of the sample suggested that graphitization may be the cause of this effect. Possible shortcomings in the experimental methods have been identified and elaborated, which will serve as a stepping stone for future analysis.

Preface

Working on my Master's thesis has been like a roller coaster when it comes to sense of achievement. When I started working on this topic in the fall of 2017 through my specialization project, I had the vision that in the end, I would come to a clear conclusion about whether or not diamond should be used in future semiconductor devices in harsh environments. I guess that is called being ambitious. Most of the courses I have taken during my studies have been related to different fields of theoretical physics, so semiconductor physics was quite new to me. As a person with an inherent curiosity towards understanding the cause of every effect, it came to my attention that this project was way more comprehensive than I was able to grasp in the beginning. The feeling I am left with, can best be explained by Einstein's famous quote: *"The more I learn, the more I realize how much I don't know."* I can safely say that I have learned more in the past year than I did the first four years of my studies combined. I am sincerely grateful for all the people that has helped me and given my new insight and perspectives. I am also grateful for the career opportunities this project has led to and the motivation it has triggered within me to pursue a career in research in the future.

Acknowledgements

I would like to thank my supervisor Justin Wells for taking me on as one of his master students, as well as guidance and support throughout the semester. I would also like to thank Alex Schenk for helping me out at the lab, engaging in fruitful discussions about whatever questions I might have, and his invaluable guidance and patience. To Alex Pakpour-Tabrizi i will also like to extend my gratitude for setting aside time during his short visit to Trondheim to discuss my project. Roger Birkeland has also shown great interest in my project, and helped out whenever I needed it, as well as providing support to attend space-related conferences. Last but not least, I would like to thank Steve Apollo Yianni for making the diamond devices and guiding me through the fabrication process, as well as allowing me to intentionally destroy them.

Contents

1 Introduction

Space is a rough environment for electronics due to highly energetic particle radiation. Because of this, electronic devices for space applications have traditionally been subjected to space qualification processes which is both expensive and time consuming, and often results in outdated technology at the time of launch. With an increasingly commercialized space industry, the need for a cheaper, quicker, and thus more general solution for radiation hardened electronics arise. Commercial-off-the-shelf (COTS) electronics are both cheap and easily accessible, but they are often silicon based, which are highly susceptible for radiation damage [1]. This often increase the demand for redundancy, which in turn will affect space and power requirements. Thus, the use of COTS electronics serves as a compromise for many low-budget space missions with the cost of reduced reliability and lifetime of the spacecraft as well as a possible increase in complexity. This encourages the development of semiconductor materials with inherent radiation hardened properties. Diamond is a physically hard material which has both high thermal conductivity and breakdown field. This means that they can sustain high power and operate in environments of extreme temperatures and radiation [2]. For this reason, diamond based semiconductors seems promising as substitute for traditional semiconductor materials for electronic devices in future space missions. In order to investigate to what extent diamond devices can endure the harsh radiation environment in space, it is necessary to get a better understanding of how the devices will react to the particle exposure that can be expected.

1.1 The Van Allen Radiation belts

Many satellite orbits passes through the Van Allen radiation belts. These belts constitutes high-energy particles originating from solar winds and cosmic rays that are trapped in the magnetic field surrounding Earth. They are composed of high fluxes of protons up to energies of $\sim 100\,\mathrm{MeV}$ and electrons up to $\sim 5\,\mathrm{MeV}$. The fluxes for different particles at different energies depends on altitude. The highest fluxes of electrons is found for energies $\sim 500\,\mathrm{keV}$, while for protons it is about $100\,\mathrm{keV}$ [3]. Figures 1 and 2, shows the fluxes of electrons and protons at these energies for different altitudes.

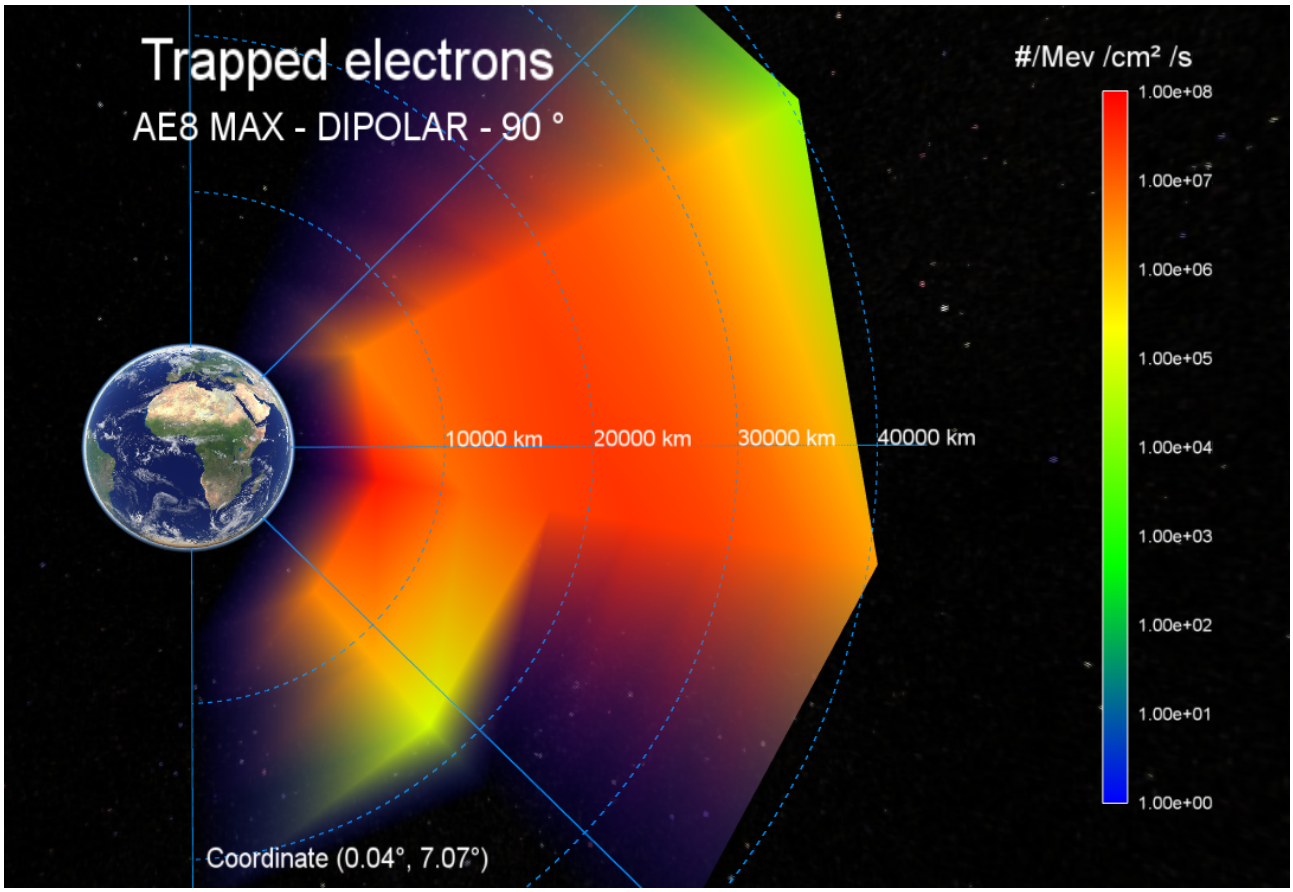

Figure 1: Meridian plot showing fluxes of electrons $\sim 500\,\mathrm{keV}$. The plot is based on reference [3].

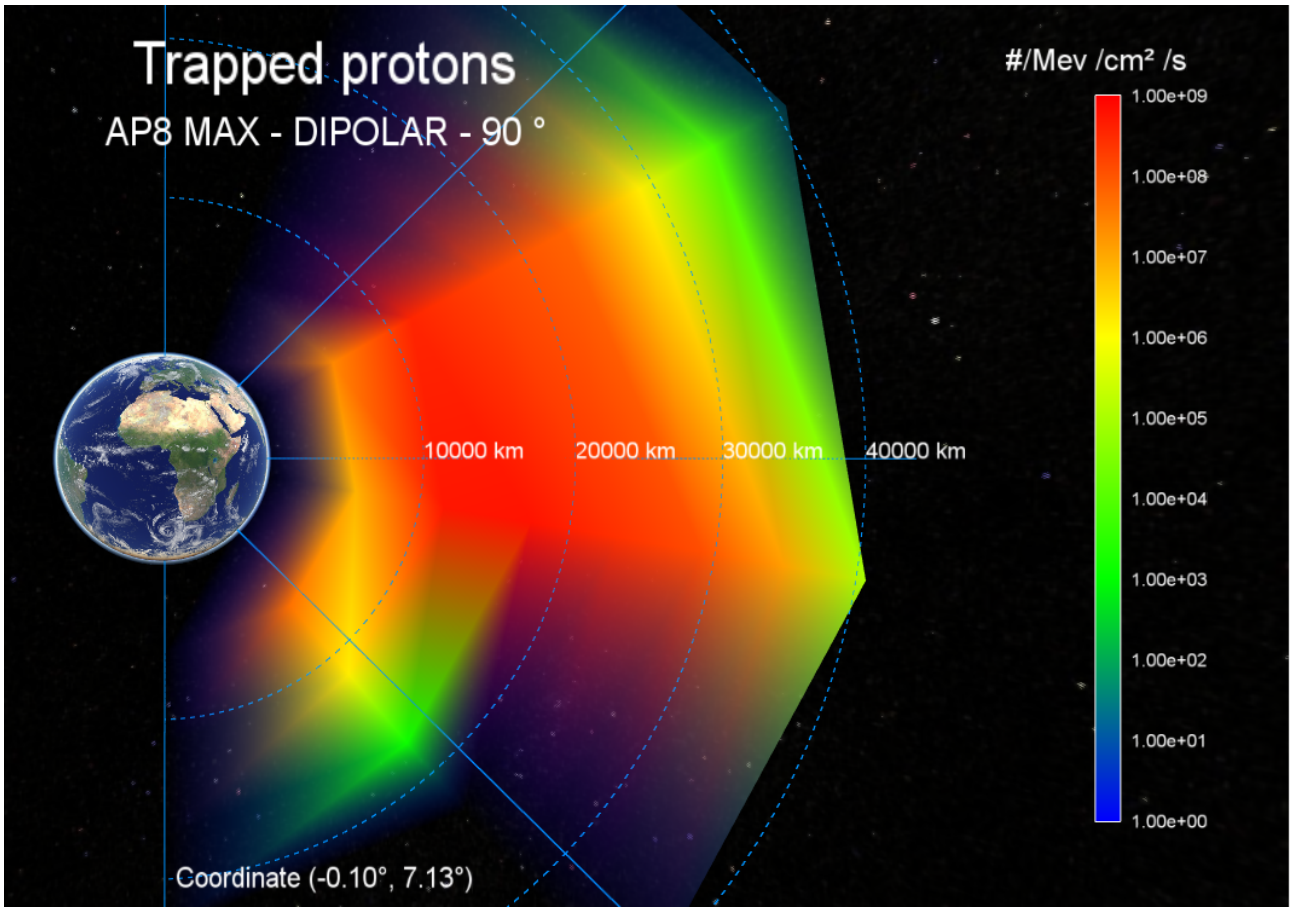

Figure 2: Meridian plot showing fluxes of protons $\sim 100\,\text{keV}$. The plot is based on reference [3].

How different devices react when exposed to this environment is a complex problem, and extremely important when designing a spacecraft. The exposure does not only vary for different orbits and orbital positions, but it is also dependent on material properties, incident angle of the particle and the position of the device within the spacecraft. This is due to the fact that particles will lose energy to a various extent prior to reaching the device, upon subsequent collisions with surrounding matter. In order to get a better idea about how a new type of device would perform in space, one has to start by looking at the material properties of that device, and what type of effects that may be induced by energetic particles under different conditions.

1.2 COTS Transistors

Transistors are used for signal amplification, switching and digital logic and serve as fundamental building blocks of all modern electronic devices. The most widely used type of COTS transistors are silicon based *metal-oxide-semiconductor field-effect-transistors* (MOSFET). However, they are also among the components that are very susceptible to radiation damage. One of the main effects of radiation on these devices is *displacement damage* in the semiconductor material. This type of defect can change the doping concentration or induce mid-gap states, which will change the electrical properties and behaviour of a transistor. Over time, this cumulative effect may alter the switching functionality of a device, which may have major implications for the operation of on-board datasystems [4]. The aim of this thesis is to investigate how these effects are manifested in diamond, in order to create a better foundation to determine whether or not diamond is superior to common semiconductor materials for space electronics.

1.3 Objectives

This thesis will focus on investigating the different effects that may be caused by radiation in diamond, and the theoretical principles behind them. The diamond devices to be investigated in are called *diamond Hall bars*. These devices exhibit surface conductivity, due to a thin layer of hydrogen deposited at the diamond surface that allows electrons to transfer from the substrate and into an adsorbate. The adsorbate is usually water, which naturally forms on the surface when exposed to the atmosphere. However, as water is easily evaporated, MoO_3 will be deposited as a more stable alternative. The change in conductivity of the devices upon exposure

to electron and helium ions will be investigated using 4-point measurements. In addition, the possible origins of altered electrical properties will be explored through photoemission experiments and Raman analysis.

2 Diamond Devices

Intrinsic diamond is an insulator with a band gap of $E_G = 5.5$ eV, but it is possible to dope it to make it conducting. One option is to dope the bulk of the diamond substrate, but so far the process is both complicated and expensive due to the small lattice spacing and large band gap of diamond. It is therefore not necessarily the right path towards large scale production of diamond-based electronic devices. However, there is another option which does not involve the introduction of dopants into the diamond lattice. *Surface transfer doping* is a way of "doping" the surface of the substrate, which allows for a p-type *surface conductivity* [5]. In order to describe the mechanisms behind surface transfer doping, it is necessary to introduce a set of *surface properties* that describes the behaviour of electrons close to the interface between two materials.

Electron Affinity
When an electron in a semiconductor excited from the valence band to the conduction band it is not able leave the material. This is due to the energetic barrier of a few eV it encounters at the surface, namely the *electron affinity*. The electron affinity χ of a material is defined as the energy required to move an electron from the *conduction band minimum* E_C inside the material, to the vacuum level E_{VAC} just outside the surface. At the vacuum level the electron has just enough energy to be considered as a free electron [6].

$$\chi \equiv E_{VAC} - E_C. \tag{1}$$

Ionization Energy
The *ionization energy* I is defined as the energy required to excite an electron from the *valence band maximum* E_V to the vacuum level,

$$I \equiv E_G + \chi. \tag{2}$$

It is can thus be interpreted as the energy required for a dopant to make a charge carrier available for conduction. The electron affinity and the ionization energy thus yield information about the energy barrier that prevents charges from leaving the material, which makes them highly dependent on surface termination. In the context of semiconductors they are used to estimate the band bending that occurs at near the interface between two materials, which describes the energy barrier charges have to overcome in order to transfer from one material to another. These quantities can be determined from photoemission experiments which will be described in detail in section 4.1.3. Since there is no way of knowing whether a photoelectron comes precisely from the conduction band minimum or the valence band maximum in these experiments, one usually measures the *work function* and *binding energy*. These energies are relative to the Fermi level, which is a statistical value.

Work Function
The work function Φ is the energy required to move an electron from the Fermi level E_F to the vacuum level just outside the surface,

$$\Phi \equiv E_{VAC} - E_F. \tag{3}$$

Since the electrons inside the material comes from the Fermi level on average, the work function thus represents the average energy barrier into free space that prevents an electron from escaping the material. It is however not a material constant, as the Fermi level depends on the doping of the material [7].

Binding Energy
The binding energy E_B represents the position of the C1s core level below the Fermi level, i.e. $E_B = E_F - E_{C1s}$, where the position of the C1s core level with respect to the valence band maximum is known to be $E_V - E_{C1s} = 283.9 \pm 0.1$ eV [8]. The binding energy is therefore an indirect measure of the position of the Fermi level within the band gap.

$$E_F - E_V = E_B - 289.3. \tag{4}$$

The relationship between these quantities can be visualized in Figure 3.

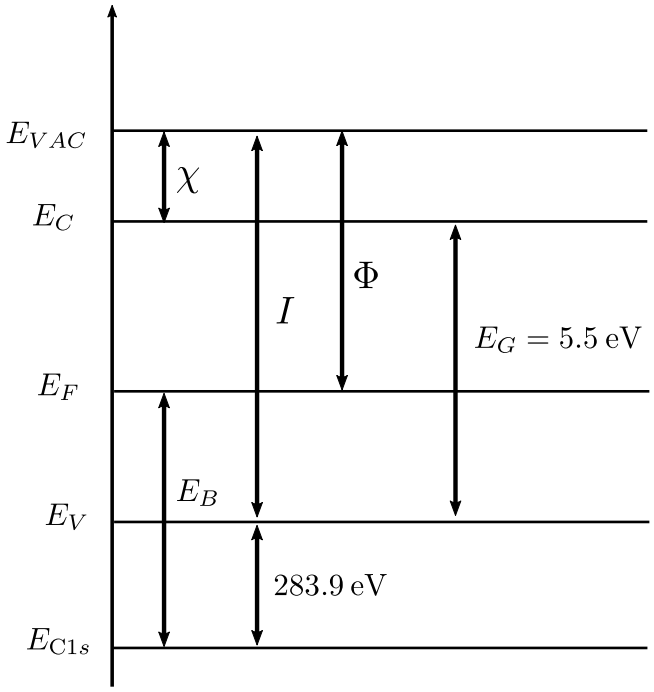

Figure 3: Band diagram for diamond showing the relationships between the work function Φ, electron affinity χ, ionization energy I and binding energy E_B.

2.1 Hydrogen Terminated Diamond

Intrinsic diamond has a *positive electron affinity* (PEA) of $\chi = 0.4\,\text{eV}$ which prevents electrons from leaving the material. However, by terminating the diamond surface with hydrogen, the electrons will be pulled slightly towards the C-H interface leaving the hydrogen surface slightly positive (δ^+) and the diamond surface slightly negative (δ^-). This is due to the fact that hydrogen has a lower electronegativity than carbon. These surface dipoles provides a potential step that pulls the vacuum level E_{VAC} below the conduction band minimum E_C leading to a *negative electron affinity* (NEA) of $\chi = -1.3\,\text{eV}$. This is quite outstanding, as a true NEA has only been observed for diamond so far [5]. To form conducting paths only in specific regions of the surface, one can make the rest insulating by terminating with oxygen. As oxygen has a higher electronegativity than carbon, this will increase the PEA with respect to the non-terminated surface to a value of $\chi = 1.7\,\text{eV}$ [8]. These mechanisms are illustrated in Figure 4.

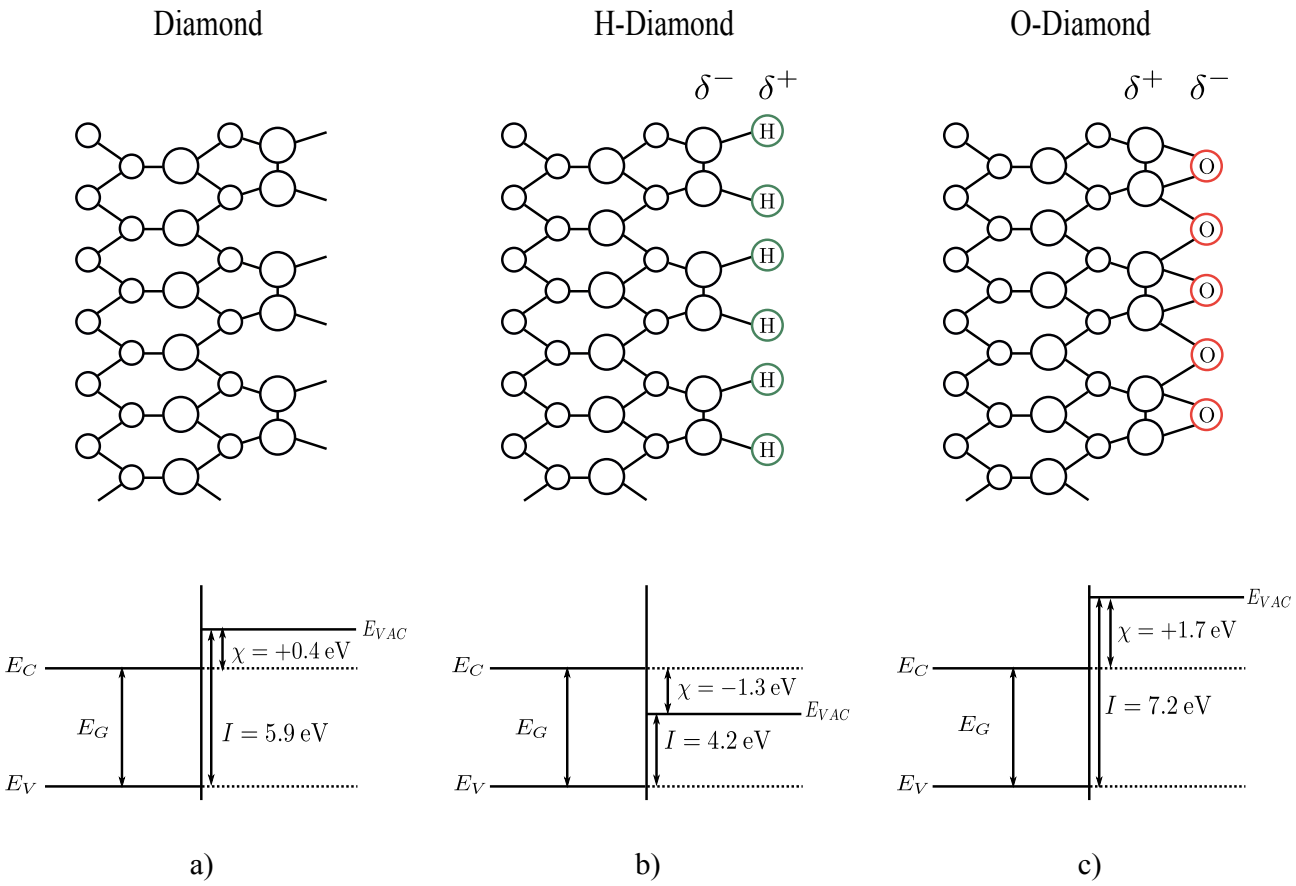

Figure 4: a)Diamond has an initial PEA of 0.4 eV. b) Hydrogen termination of the surface pulls the vacuum level below the conduction band minimum, which results in a NEA of −1.3 eV. c) Oxygen termination of the surface raises the vacuum level with respect to the conduction band minimum, yielding a PEA of 1.7 eV. - Illustration adapted from reference [9].

Hydrogen termination of the surface provides the required energy level alignment to allow a transfer of electrons from the diamond surface, but that alone does not give rise to surface conductivity. When the hydrogenated diamond surface is exposed to water in the atmosphere, electron exchange from the diamond to the water layer is governed by the redox-reaction

$$H_3O^+ + 2\,e^- \rightleftharpoons H_2 + 2\,H_2O. \tag{5}$$

The reaction is driven by the difference between the chemical potential of electrons in the liquid phase μ_e and that of diamond which is the Fermi level. As long as μ_e is below E_F, electrons are being transferred from the diamond surface to the water layer, thereby reducing H_3O^+ to H_2 and H_2O. This leaves an accumulation layer of holes at the diamond surface, which in turn induces a potential that raises μ_e. The result is a bending of the energy bands, as seen in Figure 5 [10].

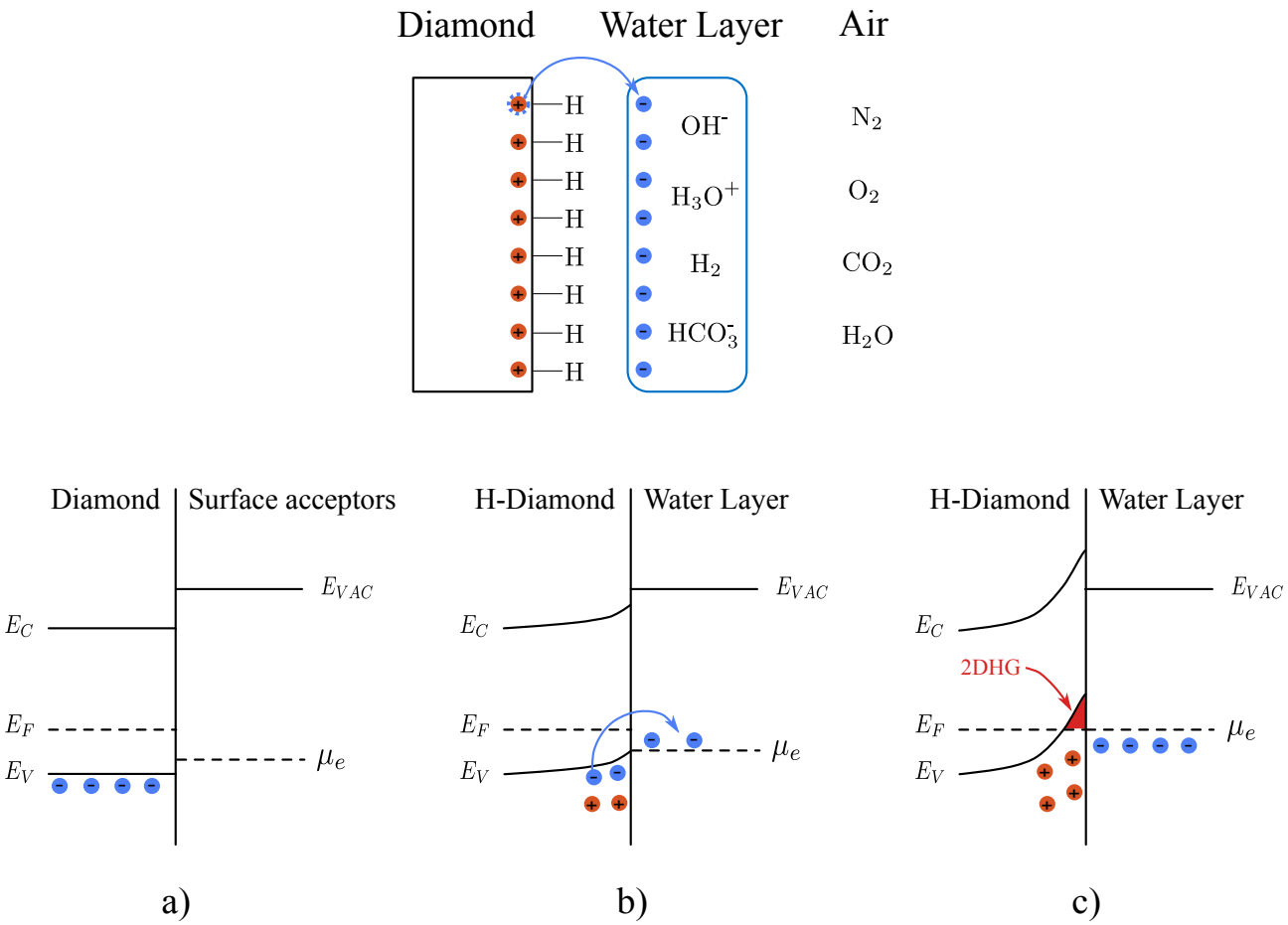

Figure 5: The process of surface transfer doping of hydrogen-terminated diamond in contact with air. a) Flat band diagram at the interface between *non-terminated* diamond and the surface acceptor (atmosphere). b) Band diagram at the interface between *hydrogen-terminated* diamond (H-diamond) and the water layer that is formed upon contact with air moisture. The upward bending bands allows electrons to transfer into the water layer, leaving holes in the H-diamond. c)A 2DHG is formed close to the interface. - Illustration adapted from reference [9].

Thus, when exposed to the atmosphere, electrons can transfer from the surface into the absorbed water layer. The hole accumulation at the diamond surface is referred to as a *two-dimensional hole gas* (2DHG). The 2DHG is what gives rise to the p-type surface conductivity. The oxygen terminated regions will remain insulating due to the PEA which prevents electrons from transferring into the water layer.
If the water layer were to be evaporated due to high temperatures, it would eventually reestablish at the surface if it is exposed to the atmosphere at temperatures where water is in the liquid phase. This has previously been demonstrated by Maier *et al.* [10]. In this study, the hydrogen termination was desorbed in one region of the sample by exposing it to an electron beam of a few keV inside a ultra-high vacuum (UHV) chamber, and masking the other part. The annealing process required to introduce samples into a UHV chamber will evaporate the water layer required for surface transfer doping, but it will eventually reestablish at the surface when exposed to the atmosphere. This was demonstrated experimentally through in-situ conductivity measurements which are illustrated in Figure 6.

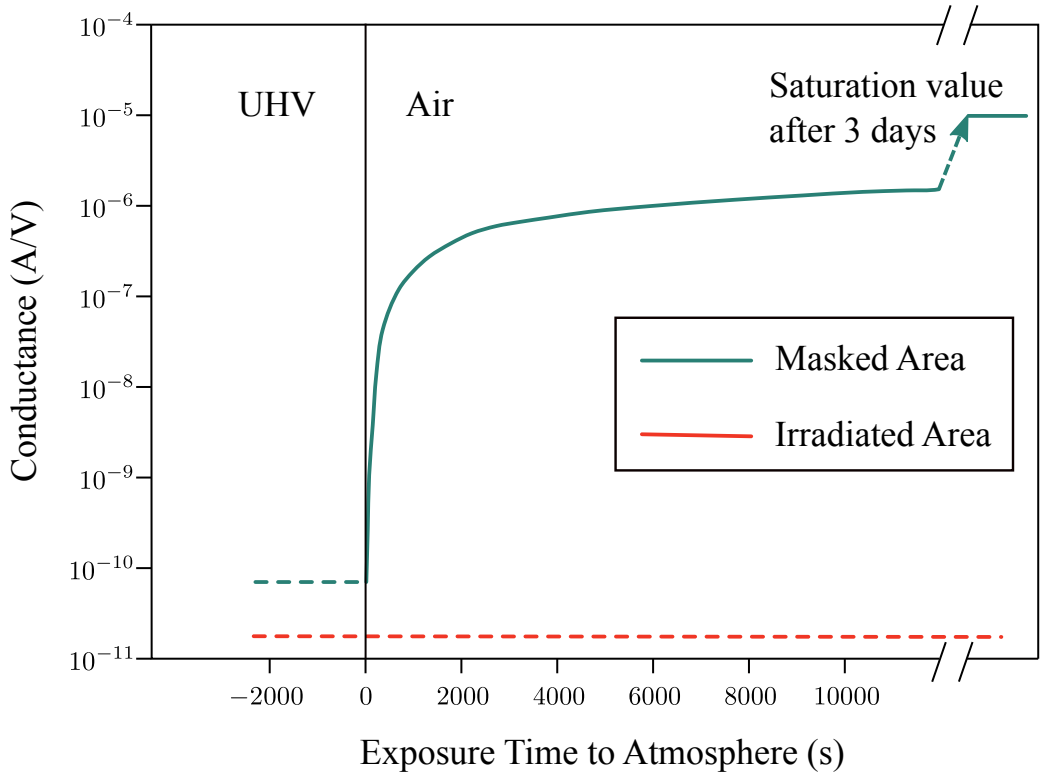

Figure 6: Surface conductance of hydrogen-terminated (masked) and hydrogen-free (irradiated) diamond during exposure to air after UHV exposure. This graph shows that after ≈ 1 hour, the masked region will have fairly stable conductivity. However, the surface will not be fully saturated until after ≈ 3 days. - Illustration adapted from reference [10].

The graph shows that both the masked and exposed areas incorporate insulating properties while inside the UHV chamber. As soon as the sample was reintroduced to the atmosphere, the masked device showed increasing conductivity, while the irradiated part remained insulating. This proves that both hydrogen termination and water is required for surface transfer doping to occur. Thus, due to the lack of atmospheric humidity in space, it would be risky to rely on water as an adsorbate in this environment. Several research articles suggests that high-electron affinity (acceptor) materials such as molybdenum trioxide (MoO_3), serves as a superior adsorbate for surface transfer doping in the sense that they have a higher boiling point, and are generally more stable. A number of these studies also conclude with increased carrier density upon MoO_3 deposition, compared to that obtained with water [11][12][13]. For this reason, the effect of MoO_3 deposition on these devices will be investigated.

2.2 Diamond Hall Bars

In order to use hydrogen terminated diamond for device applications, it is necessary to form *Ohmic* metal-semiconductor contacts at the surface. Palladium is used for this purpose due to its adhesive nature, low resistivity at low temperatures and thermal stability [14]. The contacts are placed in a six-contact (1-2-2-1) Hall bar geometry. This allows for *Hall effect* measurements, which makes it possible to determine the carrier density and mobility of the device [15].

2.2.1 Diamond Samples

The diamond devices have been manufactured by Steve Apollo Yianni at La Trobe University in Melbourne, Australia. For the samples they use a type IIa single crystal diamond(100) substrate provided by Element Six. Type IIa diamonds are the purest type of diamond, and they also have the highest thermal conductivity [16]. These are produced by chemical vapour deposition (CVD), as natural diamonds are rare and usually has high impurity densities. Each sample is 500 μm thick and has a surface area of 4.5×4.5 mm. The substrate is exposed to hydrogen plasma while annealing which allows for C-H bonds to form at the surface. UV photolithography is used in order to form hydrogen and oxygen terminated regions in a specific Hall bar geometry. In short, this method can be summarized in four steps:

- **Coat the sample surface in a positive photoresist and anneal it:** A positive photoresist is a light

sensitive material which when exposed to light becomes soluble in a developer. By annealing it, the solvent content is reduced and the adhesion, sensitivity and resistance towards deforming forces is improved.

- **Expose the sample to UV light through a mask:** The mask has the shape of the desired Hall bar geometry, which means that everything except the "Hall-bar-region" will become soluble.
- **Develop the sample in a developer:** The developer will remove the UV exposed photoresist.
- **Expose sample to oxygen plasma:** All regions except for the Hall-bar-region, which still has the photoresist intact, will become oxygen terminated.

The formation of the contacts is done in a similar manner, using a mask that defines the geometry of the contact pads, and deposition of palladium instead of oxygen. The thickness of the Pd contact pads is $\sim 120\,\text{nm}$. They are placed such that they cover parts of the hydrogen-terminated Hall-bar-region as illustrated in Figure 7. Four of these Hall bars have been created on each sample.

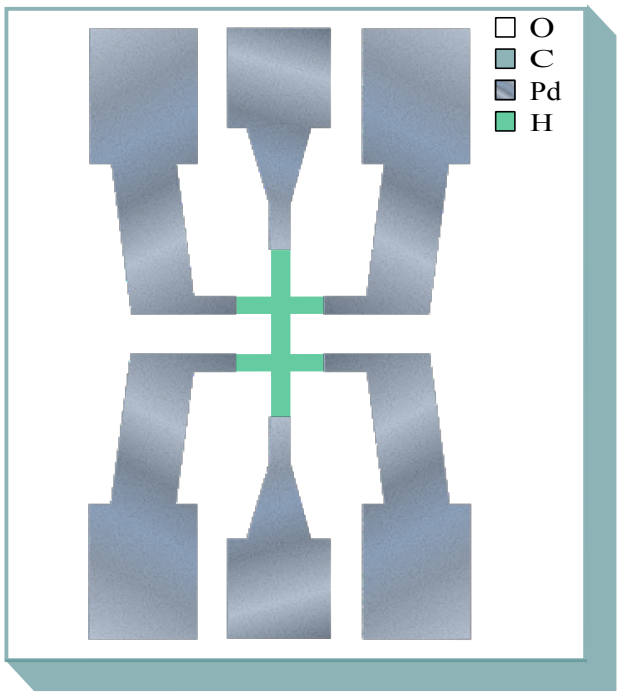

Figure 7: Geometry of the diamond Hall bars. The hydrogen-terminated regions extends underneath the palladium contacts.

These Hall bars are made for research purposes only. For reference, it it possible to make p-type field-effect transistors (FET) based on the same principles but with a different geometry, which is shown in appendix A [17].

2.2.2 Hall Effect

General Concept
If a magnetic field B is applied perpendicular to the current through a conductor, the moving charge carriers will be influenced by a transverse magnetic force F_m which will deflect the charges in a direction transverse to the current

$$F_m = qv_dB, \tag{6}$$

where q is the charge, v_d is the drift velocity, and B is the magnitude of the magnetic field. Since the current I through the conductor is given by

$$I = nqAv_d, \tag{7}$$

where n is the charge carrier density and A is the cross sectional area of the conductor, the magnetic force can be expressed as

$$F_m = \frac{eIB}{nA}. \tag{8}$$

This force will push the charge carriers to one side of the conductor. A buildup of charge at the sides of the conductor will result in an increasing electric force F_e

$$F_e = qE = \frac{qV_{xy}}{w}, \tag{9}$$

where w is the width of the conductor and V_{xy} is the induced transverse electric potential called the *Hall Voltage*. This is called the Hall effect, and is illustrated in 8.

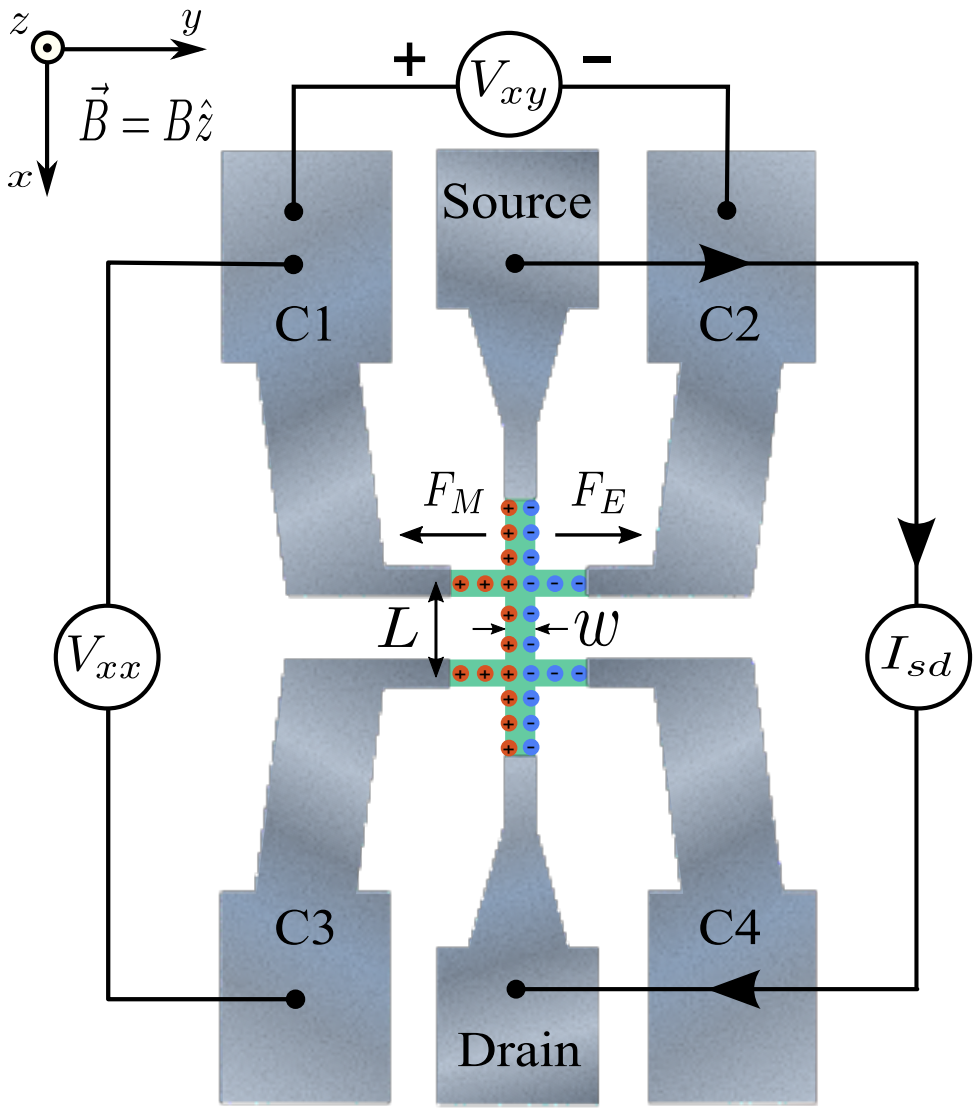

Figure 8: A sketch of the hall effect with a magnetic field B applied in the z direction. Also shown is the measurement positions for V_{xx} and V_{xy}. The width of the channel is $w = 40\,\mu$m, and the length is $L = 200\,\mu$m [18].

At equilibrium $F_m = F_e$, which yields an expression for the charge carrier density n

$$n = \frac{IB}{qdV_H}, \tag{10}$$

where d is the thickness of the conductor. Thus, by measuring the induced Hall voltage, one can determine the charge carrier density, which is an important electrical property for a transistor.

Conducting Sheets

The resistance R of a three-dimensional material is given by

$$R = \frac{V}{I} = \rho\frac{L}{wd} \tag{11}$$

where ρ is the *bulk resistivity* and L is the length of the conductor.
For a two-dimensional geometry such as the 2DHG channel on the devices to be investigated in this project, the current will flow along the plane of the termination layer rather than through the bulk of the device. Thus, the *sheet resistivity* ρ_s given by equation 12 describes the resistance of the device, i.e. how strongly the termination layer opposes a flow of current in the x-direction,

$$\rho_s = \rho_{xx} = \frac{\rho}{d} = \frac{wV_{xx}}{LI_{sd}}. \tag{12}$$

ρ_s has units of $\Omega\square^{-1}$, which is dimensionally equal to Ω, but the expression is exclusively used for sheet resistivity which is emphasized by the square unit. The interpretation of $\square^{-1}$ is that for a square sheet ($L = w$), the sheet resistivity ρ_s is equal to the resistance R regardless the size of the square.
The *Hall resistivity* ρ_H describes how strongly the termination layer will oppose a movement of carriers in the y-direction forced by a magnetic field perpendicular to the applied current in the x-direction. It is the ratio of the transverse Hall voltage V_{xy} induced by the charges deflected in the $y-direction$, and the current $I_s d$ in the x-direction,

$$\rho_H = \rho_{xy} = \frac{V_{xy}}{I_{sd}}. \tag{13}$$

However, the Hall-effect is sensitive to the alignment of the contacts used for voltage measurements. If they are slightly offset, the measured voltage will not correctly describe the parallel or perpendicular component of the electric field. Therefore an important part of the manufacturing process is to make sure that the contact pads are properly aligned. In order to account for the possible effect of this, one should perform the Hall measurements with both positive and negative applied magnetic fields [5]. The Hall resistivity can then be determined from equation 14,

$$\rho_H = \frac{\rho_H(+B) - \rho_H(-B)}{2}. \tag{14}$$

Thus, for a two-dimensional conductor, the charge carrier density in equation 10 corresponds to the *hole sheet density* n_s,

$$n_s = \frac{I_{sd}B}{qV_{xy}} = \frac{B}{q\rho_H}. \tag{15}$$

The *hole mobility* μ is a measure of how quickly a hole can move through the sheet,

$$\mu = \frac{V_{xy}}{I_{sd}B\rho_s} = \frac{1}{qn_s\rho_s}. \tag{16}$$

Thus, the *Drude conductivity* σ of the device can be computed as

$$\sigma_0 = qn_s\mu = \frac{1}{\rho_s}, \tag{17}$$

which is the reciprocal of the sheet resistivity and represents the ability to conduct [5].
It is important to note that the accuracy of the resistivity measurements are sensitive to the width of the channel and the distance between the contacts used for measuring. These are however often difficult to measure accurately [15]. A recent study by Akhgar *et al.* also suggests that hole-hole interactions will introduce a temperature dependence in the resistivity measurements [19]. These effects will not be taken into consideration here.

3 Radiation Effects in Hydrogen Terminated Diamond

There are different effects that can occur when a material is exposed to particle radiation. The observed change in properties may depend on the particle type, the energy of the particles, the dose rate and total dose, as well as temperature. For this reason, the analysis of radiation effects if quite complex, and it is therefore important to have a better understanding of some of the ways particles may interact with matter.

3.1 Inelastic Mean Free Path

When an electron passes through a material, it interacts strongly with the atoms and molecules in the solid in the form of excitations. Knowledge about how electrons interact with matter is not only important for understanding the type of damage they can induce, but also for characterization techniques based on electron detection which will be described in section 4.1.3. The inelastic mean free path (IMFP) is a measure of how far into a material an electron penetrates on average between successive inelastic collisions, which causes it to lose most of its energy. The IMFP thus depends on the energy of the incident electron and the material under consideration. By definition, it is the distance a beam of electrons can travel before its intensity is reduced to $1/e$ of the initial value. The intensity I of an electron passing perpendicularly through a solid of thickness t will decay according to Beer Larmbert's law

$$I(t) = I_0 \exp\left(\frac{-t}{\lambda(E)}\right), \tag{18}$$

where I_0 is the intensity of the primary electron and $\lambda(E)$ is the IMFP for a given energy [20]. The IMFP of electrons in diamond is has been estimated by Tanuma et al. for electron energies between 50 eV and 30 keV. Using the NIST database for IMFP, the values for MoO_3 can be obtained for energies between 50 eV and 2 keV. It has also been demonstrated that the IMFP is close to linear in the range 100 eV to 100 keV for many compounds [21]. Thus, linear extrapolation of these IMFPs up to 200 keV serves as a good approximation in order to predict how far electrons in space will penetrate into the devices, and where most of the damage will occur. This illustrated in Figure 9.

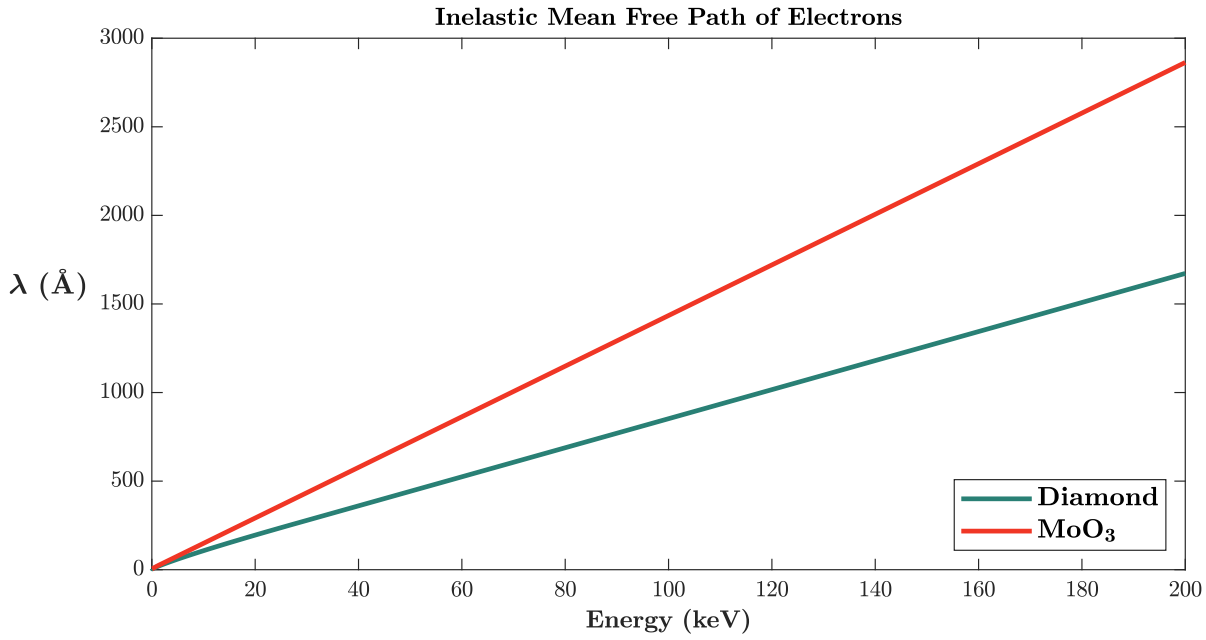

Figure 9: Linear extrapolation of inelastic mean free paths for electrons in diamond and MoO_3 from references [22] and [23] respectively.

3.2 Electron-Stimulated Desorption

The constituent electrons of the outer radiation belt may cause damage to the hydrogen-terminated diamond in terms of electron-stimulated desorption (ESD). If we consider an electron of energy $E \approx 3.5$ keV and mass $m_e = 9.11 \cdot 10^{-31}$ kg that collides with a free particle of mass $M \gg m_e$, the maximum energy transferred (ΔE) can be estimated to $\Delta E/E \approx 2m_e/M$ using classical kinematics. Hydrogen has a mass $M_H = 1.67 \cdot 10^{-27}$ kg, which means that about 3.8 eV would be transferred to the hydrogen atom in this case. However, previous research has shown that also molecules and atoms of greater mass can be desorbed by electrons with energies less than 10 eV. This suggests that direct momentum transfer is not the only mechanism responsible for ESD, and that also electronic energy transfer must be taken into consideration. In addition, due to the strong bond energies of many chemisorbed surface adsorbates, one usually treats desorption caused by low-energy electrons in terms of electronic excitation mechanisms. The C-H bond on (100) diamond is ~ 4.5 eV , and the density of

carbon atoms at the surface is about $1.6 \cdot 10^{15}\,\mathrm{cm}^{-2}$ [24][25]. For a flux density of $\sim 10^{13}$ electrons $\mathrm{cm}^{-2}\mathrm{s}^{-1}$, the probability of a simultaneous interaction between a hydrogen atom at the surface and more than one primary electron is small. Based on these considerations, the mechanisms behind ESD is understood by treating electron-adsorbate scattering as isolated events, where the electronic energy transfer plays the predominant role [26]. Thus, exposure to electrons of of a few keV may eventually desorb the hydrogen layer, which has also been demonstrated by Maier *et al.* [10]. The energies encountered in space are usually much higher which means that most electrons are likely to pass through the surface with little effect due to the long IMFP. However, there is reason to believe that some portion of the electrons may have a reduced IMFP due to energy loss, which will cause them to deposit their energy close to the surface and induce desorption over time.

3.3 Stopping Range of Ions in Matter

The energy loss and stopping range of ions in matter (SRIM) is important for radiation damage analysis. The *stopping power* is the average energy loss per unit length (eV/cm) of an ion travelling through a material. It depends on the type of ion, its energy and the material it interacts with. The range an ion can travel through a given compound before coming to rest is therefore directly related to the stopping power. Even though the ion will lose energy along its path, most of the energy will be deposited in a small volume around the depth where it comes to rest. It is therefore important to know the stopping range of ions in diamond in the relevant energy regime, in order to predict where and what type of potential damage is most likely to occur. The *transmission of ions in matter* (TRIM) software developed by Ziegler *et al.* calculates stopping ranges based on ion species and energy, as well as information about the target or material [27][28]. In order to get an estimate of how far into the sample the protons in space would penetrate, TRIM was used to calculate the stopping range of hydrogen ions in diamond in the energy range $1 - 100\,\mathrm{MeV}$. Since helium ions will be used in the experiments which will be described later, the data obtained for both H^+ and He^+ ions in diamond is shown in Figure 10.

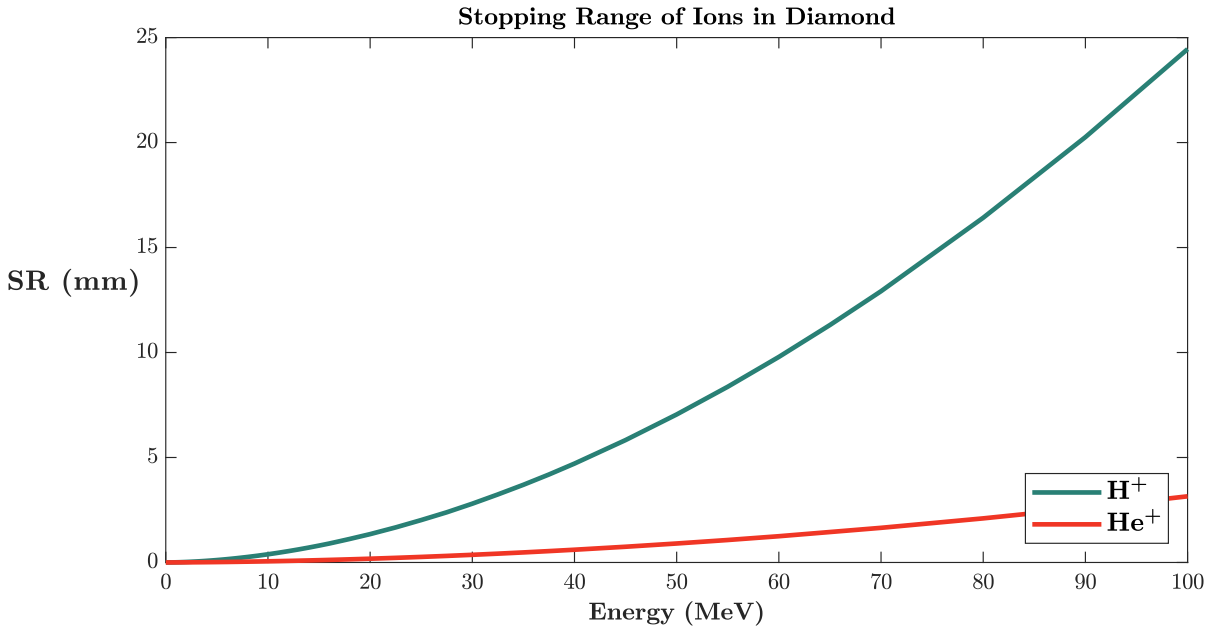

Figure 10: Stopping ranges of H^+ and He^+ ions in diamond, which shows that *most* protons in space will pass through the devices.

Even though most of the protons in space would pass through the device, they may cause graphitization for sufficiently high doses. In addition, ions of lower energy that are present, may cause *ion-stimulated desorption* (ISD) over time. This effect may be induced by many of the same mechanisms as for ESD [29].

3.4 Graphitization

Graphite is a more stable form of carbon than diamond. When a sufficient number of the sp^3 diamond bonds are broken, the carbon atoms may rearrange and form sp^2 graphite bonds, leaving delocalized electrons available for conduction. This different bonding configuration of the carbon atoms causes graphite and diamond to have very different physical properties. While pure diamond is a wide band-gap and thus insulating material,

graphite is highly conductive. Depending on the circumstances, ion bombardment of diamond may *graphitize* regions within the diamond structure, which may lead to a change in the electrical behaviour of the device. The change in electrical resistance R upon ion bombardment of diamond depends on the implantation temperature T_i, dose D and ion type. Kalish *et al.* showed through in-situ measurements that diamond exposed to a 100 keV carbon ion beam at $T_i = 490\,\mathrm{K}$, yielded a sharp drop in resistance at a total dose of $D \sim 10^{16}$ ions/cm^2 [30]. This is referred to as the *critical dose* D_c, which is the dose at which the diamond lattice is destroyed and graphitization occurs. For doses below D_c, it may be possible to restore the partly damaged diamond lattice by thermal annealing. On the other hand, for doses above D_c thermal annealing will result in complete graphitization. For reference, 100 keV carbon ions has a stopping range of $130 \pm 22\,\mathrm{nm}$ in diamond. A similar measurement was performed for 320 keV xenon ions which has a stopping range of $56 \pm 9\,\mathrm{nm}$ in diamond. This yielded a critical dose of $\sim 10^{15}$ ions cm^{-2} for the same T_i. The shape of the $R(D)$ curves proved to be almost identical for the two species, only scaled to higher doses for the lighter and less energetic carbon ion. This suggests that the change in resistance does not depend on the ion species, but rather on the amount of damage each ion creates. This can be expressed in terms of the energy density Q deposited per ion

$$Q = \frac{nE}{(R_p + \Delta R_p) \cdot 1.76 \cdot 10^{23}}, \tag{19}$$

where n is the fraction of energy lost by nuclear collisions, E is the ion energy in eV, R_p and ΔR_p are the range and straggling of the incident ion, and $1.76 \cdot 10^{23}$ atoms/cm^3 is the atomic density of diamond. n, R_p and ΔR_p can be calculated for all ions in TRIM [27]. The critical dose is not only dependent on the ion type and energy, but also on the implantation temperature. Due to dynamic annealing effects, the critical dose increases with increased implantation temperature. Thus, for sufficiently high T_i, graphitization can be completely avoided [31]. The mechanism behind graphitization can be understood by considering a single ion striking the diamond sample. As the ion passes through the material, it generates a "thermal spike" surrounding its track, which lasts for about 10^{-12} s. As a result, it leaves in its wake highly defect regions with many broken bonds. These defect regions can be imagined as spheres of average radius r_0 which randomly scatter along the track. During a diffusion time $\tau \approx 10^{-9}$ s, the displaced atoms and vacancies in these defect spheres may recombine to form a sheath of thickness δr, leaving a stable defect sphere of radius $r_0 - \delta r$. At low T_i, the diffusion of defects is inhibited, and $\delta r = 0$. On the other hand, at high temperatures, $\delta r = r_0$, and the damage sphere is dynamically annealed. The resulting radius of the defect sphere may thus be expressed as a function of T_i

$$r(T_i) = r_0 \left[1 - B\exp\left(\frac{-U}{k_B T_i}\right)\right]. \tag{20}$$

Here, $U = E_{df}/2$, where E_{df} is the activation energy for defect diffusion and k_B is Boltzmann's constant. B is a constant depending on the stopping power of the incident ion, the diffusion time τ, the number of target atoms/cm^3 and on the displacement energy. When the density of these spheres reaches a sufficient concentration they will overlap and form a conductive pathway along the trail, as seen in Figure 11.

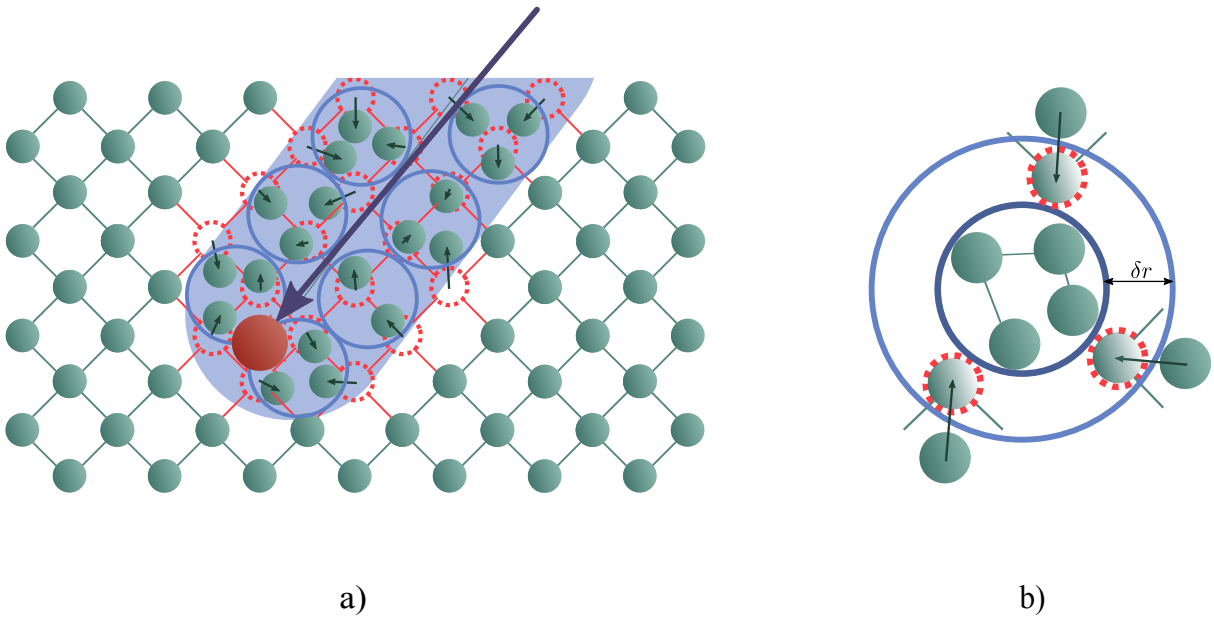

Figure 11: a) An ion strikes the diamond, inducing a thermal spike which creates unstable disordered regions clustered together in a sphere of radius r_0. The red lines are the resulting dangling bonds, and the red dotted circles are vacancies. b) During a time $\tau \approx 10^{-9}$ s, the vacancies inside a sheath of thickness δr of the sphere diffuse, and the region is recrystallized. A stable amorphous region is then formed inside the sphere of radius $r_0 - \delta r$.

Thus, the decrease in D_c with increasing T_i can be visualized as the damage spheres shrinking due to thermal annealing of the defects. Furthermore, it was shown that the *dose rate* (ions/cm^2/s) also has an effect on the critical dose. As the dose rate increases, there is an increased probability of defect regions overlapping before defect annihilation occurs. The critical dose will therefore decrease with increasing dose rate. These effects can be interpreted as the diamond equivalent of displacement damage in traditional semiconductor materials, which can be caused by ions, as well as protons and neutrons in space. If conductive paths of graphite extending from the sub-surface region within the 2DHG and into the diamond substrate is formed, it can cause leakage currents which may limit the device performance.

4 Experimental Methods

In order to investigate the effects of particle irradiation, a combination of different characterization techniques and irradiation experiments is required. In order to fully understand the obtained results and interpret possible ambiguities, it is important to understand the mechanisms behind each of the experimental methods used.

4.1 Characterization

As there are usually several possible causes of an observed change, various ex-situ characterization measurements were performed to create a solid basis for interpretation. This involves contact characterization, *I-V* measurements, photoemission analysis and Raman spectroscopy.

4.1.1 SEM

Due to extensive and adverse treatment of the devices, they all have some damage to their contact pads originating from e.g. previous wire-bonds and tweezer scratches. In order to investigate the condition of the palladium contact pads and thus determine the devices more suitable for *I-V* measurements, a *scanning electron microscope* (SEM) was used to produce high resolution images of the samples. SEM is a technique focuses a beam of electrons onto the sample and performs analysis of the backscattered electrons to produce images of nanometer scale resolution [32]. It allows zooming in and out as well as effortless maneuverability of the sample holder while using the microscope. However, due to the fact that the devices are sensitive to low-energy electrons, it is important to keep the exposure time at a bare minimum. The microscope was set up in analy observation mode which yields high-contrast images [33].

4.1.2 Four-Point Measurements

As discussed in section 2.2.2, a combination longitudinal and transverse of current-voltage (I-V) measurements is needed in order to determine the hole mobility μ, sheet density n_s and conductivity σ_0 of the devices. In order to minimize the error due to contact resistance, four-point measurements are used for the I-V measurements. The technique relies on applying a current between two *force* connections of a Source Measure Unit (SMU), which will generate a voltage drop across the channel. By measuring the voltage between a pair of *sense* connections placed *between* the force connections, it is possible to eliminate the voltage drop in the force contacts, and measure only the voltage drop across the conducting channel. This arrangement is illustrated in Figure 8. Due to the small size of the devices, and the fact that they do not have wires attached to the connection pads, the measurements is performed by connecting four *MiBots* to the SMU. A MiBot is a micromanipulator, which can move freely and precisely on a surface. The speed and precision can be controlled by adjusting the amplitude and frequency of movements in each direction. They have a controllable arm to which it is possible to attach probes of different sizes, as seen in Figure 12.

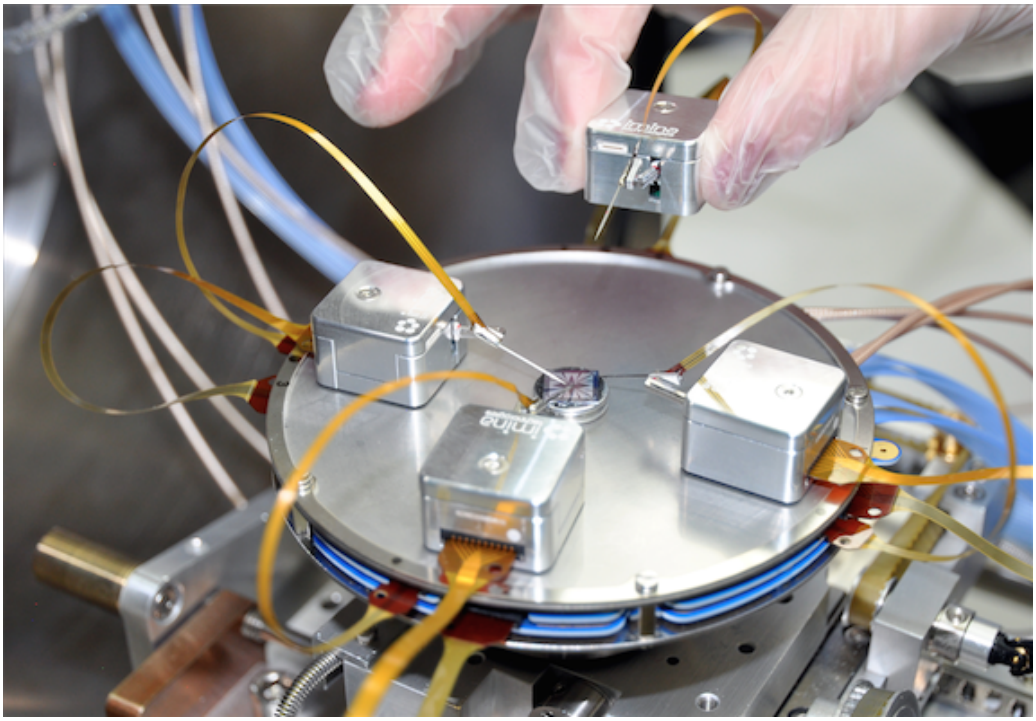

Figure 12: MiBots - Photo by Imina Technologies [34].

By placing the MiBots under an optical microscope it is easy to maneuver the probes onto the connection pads of the Hall bars as seen in Figure 13.

Figure 13: Micromanipulator probe positions for Hall voltage measurements.

In order to determine the sheet resistivity ρ_s, a current I_{sd} is applied by placing probes at the source and drain terminals. By placing the other two probes at contacts C1 and C3, the voltage V_{xx} can be measured.
The Hall resistivity ρ_H is determined in a similar manner, by measuring the voltage V_{xy} through the probes placed at contacts C1 and C2. However, to induce the Hall voltage, it is required to apply a uniform magnetic field perpendicular to the device as described in section 2.2.2. This is achieved by centering the device under test (DUT) on a small magnet, and measuring for both positive and negative field directions by flipping the magnet. The magnetic field strength of the magnet was measured to $B \approx 275$mT using a Gauss meter.

The SMU has a maximum compliance of 42 V without external grounding. As the sheet resistivity is different for every device, it is not possible to pass the same current through all of the devices without reaching this value. By performing a test-measurement on one of the least damaged devices, an upper bound of ~ 0.75 mA for the applied current was determined. The voltage drops induced by various values of I_{sd} was then measured by controlling the SMU through a python script which sweeps the range $0.75\text{ mA} \leq I_{sd} \leq 0.75\text{ mA}$ for the applied current. The sheet resistivity ρ_S and Hall resistivity ρ_H is computed for each set of I-V values from equations 12 and 13 respectively. The hole sheet density n_s, hole mobility μ and conductivity σ_0 can then be calculated from equations 15, 16 and 17 respectively, using average resistivity values. All measurements were performed at room temperature.

4.1.3 Photoemission Spectroscopy

Photoemission Spectroscopy (PES) is a surface sensitive technique for investigating the electronic structure of a material. When irradiating a sample with photons, some atoms or molecules may absorb the photon and consequently emit electrons with a certain kinetic energy depending on the incident photon energy and material properties. This is is known as the photoelectric effect. The *maximum* kinetic energy E_k of the emitted photoelectrons is given by Einstein's photoelectric law

$$E_k = h\nu - \Phi_S, \tag{21}$$

where h is Planck's constant, ν is the frequency of the ionizing light and Φ_S is the work function of the sample. If the emitted electrons comes from an energy level of binding energy E_B below the Fermi level, equation 21 becomes

$$E_k = h\nu - E_B - \Phi_S. \tag{22}$$

Since the kinetic energy of the emitted electrons is the source of information in PES experiments, it is *necessary* to perform these measurements in UHV. This ensures that deflections and energy loss due to interactions with surrounding particles is minimized. There are two main types of PES; *ultraviolet photoemission spectroscopy* (UPS) and *X-ray photoemission spectroscopy* (XPS) differing by the photon energy used for measurements. UPS is mainly used for measurements regarding the valence band, while XPS is used for core level analysis due to the higher photon energy [35].

Ultraviolet Photoemission Spectroscopy

UPS is often used to determine the the work function of a material. A photon energy of $h\nu = 21.2\,\text{eV}$ is commonly used to excite electrons in the valence band. At this energy, the photons have a penetration depth of less than 5 nm in diamond [36]. However, the IMFP of electrons in diamond for this energy range is less than 1 nm according to the universal IMFP curve [37]. This means that only the electrons that are excited close to the surface have enough energy to escape the material and be detected. Thus, UPS is extremely surface sensitive, which makes it suitable for determining the electronic properties of these surface conducting devices. As the sample is in electrical contact with the detector during photoemission experiments, equation 22 cannot be used to determine the work function without modification. The detector has a work function Φ_D, which results in a potential difference $\Delta\Phi = \Phi_S - \Phi_D$ caused by the local vacuum level difference between the sample and the detector. Thus, the kinetic energy *measured* by the detector is given by

$$E_k^{meas} = h\nu - E_B - \Phi_S + \Delta\Phi = h\nu - E_B - \Phi_D. \tag{23}$$

This is illustrated in Figure 14 a). As the measured kinetic energy is independent of Φ_S, it is necessary to account for $\Delta\Phi$ in order to determine the work function of the sample. This can be done by calculating the width of the measured kinetic energy spectrum $E_{k,max}^{meas} - E_{k,min}^{meas}$. The maximum measured kinetic energy $E_{k,max}^{meas}$ corresponds to the kinetic energy of an electron emitted from the Fermi level. This yields the following expression for the maximum value of the kinetic energy spectrum

$$E_{k,max}^{meas} = E_F + h\nu - E_{VAC}^D \tag{24}$$

The minimum measured kinetic energy $E_{k,min}^{meas}$ originates from emitted electrons which leave the sample with zero kinetic energy, i.e. electrons that have just sufficient energy $\left(\sim E_{VAC}^S\right)$ to escape the sample. Thus, we have the following expression for the minimum value

$$E_{k,min}^{meas} = E_{VAC}^S - E_{VAC}^D. \tag{25}$$

However, it is almost impossible to detect these electrons as they do not have enough kinetic energy to make it into the detector. This is solved by applying a small negative bias V_b to the sample when measuring the minimum value, as seen in Figure 14 b) [38].
Thus, by comparison to equation 3, it is evident that

$$E_{k,max}^{meas} - E_{k,min}^{meas} = h\nu + E_F - E_{VAC}^S = h\nu - \Phi_S. \tag{26}$$

Accounting for the applied bias, the work function is expressed as

$$\Phi_S = h\nu - (E_{k,max}^{meas} - (E_{k,min}^{meas} - V_b)) \tag{27}$$

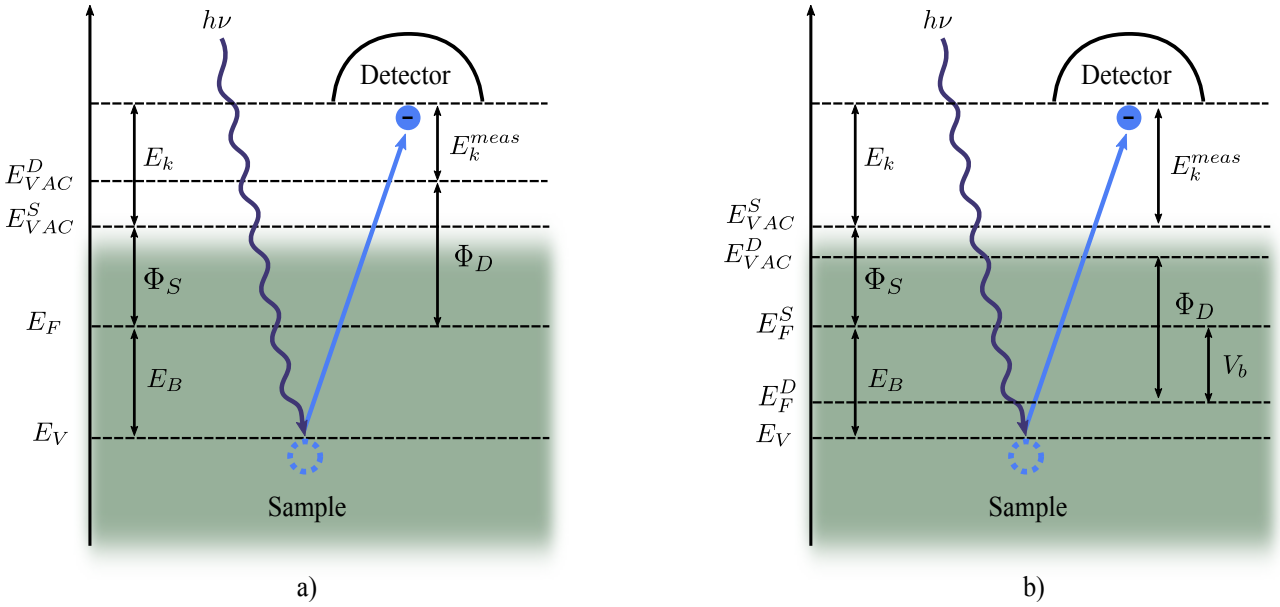

Figure 14: a)Band diagram for the UPS measurement of electrons in the *high-energy regime*. An incoming photon of energy $h\nu$ excites an electron in from the valence band. The measured kinetic energy E_k^{meas} is the energy that remains after the electron has overcome the binding energy E_B, the work function Φ_S of the sample and the vacuum level E_{VAC}^D of the detector. b) Band diagram for the UPS measurements of electrons in the *low-energy regime*. Some of the electrons excited by the photons will have just enough energy to make it to the vacuum level, where they are regarded as free electrons with zero kinetic energy. In order to detect them, they are biased by a potential V_b so that they can make it into the detector.

X-Ray Photoemission Spectroscopy

At a photon energy of $h\nu = 1253.6$ eV, XPS can be used to excite core level electrons in a material and thus determine the binding energy. By neglecting the relatively small vacuum level difference between the sample and the detector, the measured kinetic energy spectrum is given by equation 22, as illustrated in Figure 15.

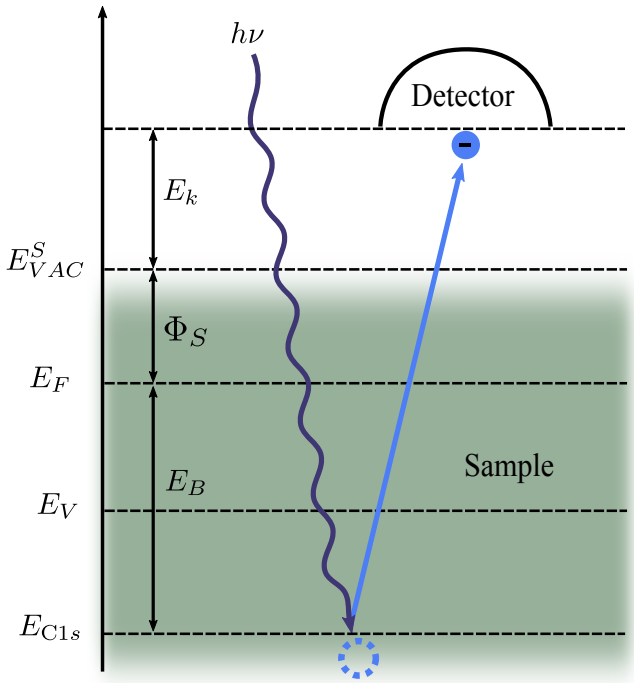

Figure 15: Band diagram for XPS measurements. An incoming photon of energy $h\nu$ excites an electron from the C1s core level. When neglecting the vacuum energy difference between the sample and the detector, the detected kinetic energy E_k is the energy that remains after overcoming the binding energy E_B and the work function Phi_S of the sample.

After the work function has been determined by UPS, it is straightforward to compute the binding energy,

$$E_B = h\nu - E_k - \Phi_S \tag{28}$$

Measuring the binding energy makes it possible determine the position of the Fermi level with respect to the valence band maximum from equation 4. The work function measurement on the other hand, determines the position of the vacuum level with respect to the Fermi level. Thus, a combination of UPS and XPS measurements can also be interpreted as a method for determining the positions of the Fermi level and the vacuum level in the band diagram, as illustrated in Figure 3. Based on equation 1, the electron affinity can then be calculated as

$$\chi = \Phi_S - (E_C - E_F) = \Phi_S - (E_G - (E_F - E_V)). \tag{29}$$

XPS and UPS measurements are performed before and after irradiation, to detect changes in the electron affinity in specific. The UPS measurements were performed by measuring at three different positions on the sample, with a bias of $V_b = 9$ V for the low-energy regime. The XPS measurements scans the whole surface, resulting in a spectrum that yields an average over the area.

4.1.4 Raman Spectroscopy

Raman spectroscopy is a method for determining the types of materials present in a sample by illuminating a sample with a laser and measuring the intensity of the *scattered* light. When light of a certain wavelength interacts with a material, the vibrations or phonons present may be excited by the photon. Most often, the vibrations will emit a photon of the same wavelength as the incident light and fall back to its initial state. This effect is called *elastic Rayleigh scattering*. However, a small portion of the photons may cause excited vibrations to relax at a level above or below the initial state. This is referred to as Stokes and anti-Stokes Raman scattering respectively, which is an *inelastic* process. The effect of Raman scattering is a red-shift of the emitted light in the case of Stokes, and a blue-shift in the case of anti-Stokes. This wavelength shift is referred to as the *Raman shift* Δw, which given by equation 30 in units of cm^{-1},

$$\Delta w = \frac{1}{\lambda_0} - \frac{1}{\lambda_1}. \tag{30}$$

Here, λ_0 is the wavelength of the incident light, while λ_1 is the wavelength of the scattered light. The underlaying mechanisms of Rayleigh and Raman scattering are illustrated in Figure 16.

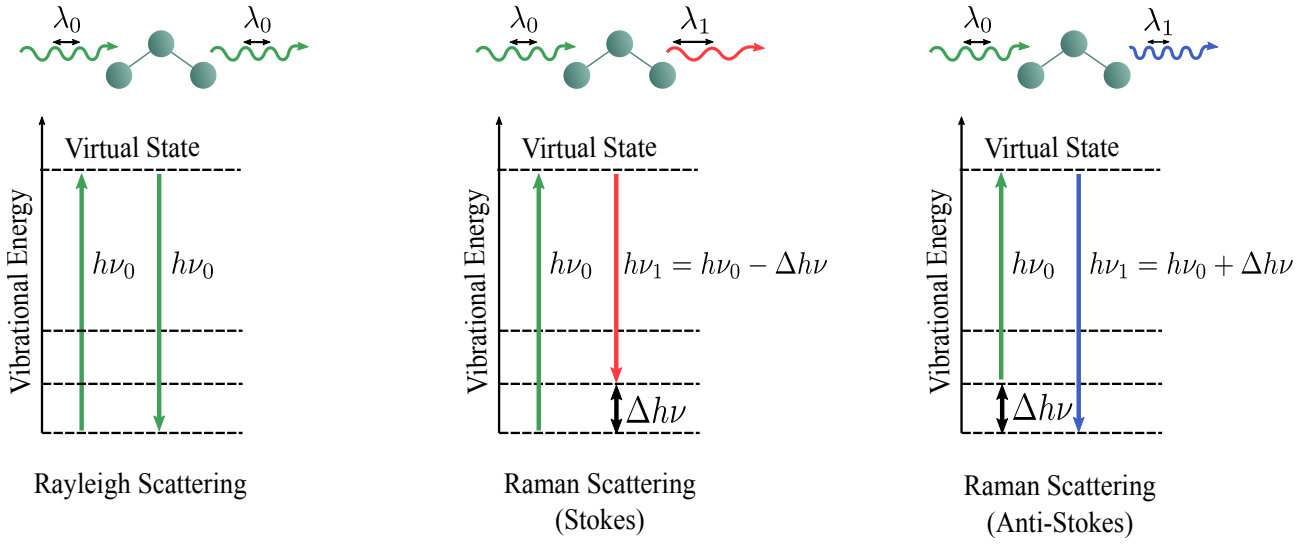

Figure 16: Principles of Rayleigh and Raman scattering. Here, $h\nu_0$ and $h\nu_1$ are the energies of the incident and emitted light respectively, and λ_0 and λ_1 are the corresponding wavelengths. $\Delta h\nu$ is the Raman shift in terms of energy (i.e. electronvolts).

The intensity of the Raman scattered light is usually very weak compared to that of Rayleigh scattering. Therefore, the elastically scattered photons with energies corresponding to the incident laser is filtered out in the spectrometer to obtain information about the energy shift of the inelastically scattered photons. The Raman shift gives information of the vibrational modes present, which is a characteristic of the material [39]. Diamond has a Raman shift of around $1332\,\mathrm{cm}^{-1}$, while graphite can be identified by the D-band ($\sim 1350\,\mathrm{cm}^{-1}$), G-band

($\sim 1580\text{cm}^{-1}$) and the 2D-band ($\sim 2700\text{cm}^{-1}$). The G-band is commonly called the *graphite-band* which results in a high peak for pure graphite Raman spectra. The reason why graphite has several bands in it spectrum is that some of the carbon bonds have different bond energies, while diamond is a lot more uniform in that sense. The D-band originates from some disorder in the graphite structure, which is why it is often referred to as the disorder- or defect-band. The intensity of this band relative to the G-band is therefore often used as a measure of graphite quality. As for the 2D-band, its intensity relative to the G-band is usually significantly higher in graphene than in graphite [40]. By performing a two-dimensional map-scan over the sample surface, Raman spectroscopy can be utilized in order to investigate possible graphitization in the diamond lattice due to ion irradiation. This method will collect spectra from points across the whole sample area, which can be analyzed by identifying possible graphite peaks for each position in the dataset. For this purpose, the Raman spectrometer was set up to scan the whole sample area with a step of 100 μm in the range $1100\,\text{cm}^{-1} < \Delta w < 3200\,\text{cm}^{-1}$. About ~ 1600 individual spectra were collected. In order check for possible graphite peaks in all of the spectra, a MATLAB script which loops through all the files was written. The approach used is illustrated in Appendix B. The laser used had an excitation wavelength of 532 nm.

4.2 MoO_3 Deposition

As discussed in section 2.1, molybdenum trioxide may serve as a better adsorbate for surface transfer doping in terms of increased stability and conductivity. In order to investigate the effect of this, MoO_3 powder was deposited on the sample surface through an evaporator. The thickness t of the deposited layer can be estimated from equation 18 by comparing the intensity of the C1s level from XPS measurements before and after deposition;

$$t = \lambda(E)\ln\left(\frac{I_0}{I}\right). \tag{31}$$

Here, I_0 and I are the areas under the C1s peak before and after deposition respectively, while $\lambda(E)$ is the IMFP for an electron of energy E in MoO_3.

4.3 Device Irradiation

Electrons and protons are both present in space, but due to their different nature, they will also cause quite different effects upon interaction with materials as discussed in section 3. It is therefore interesting to investigate the change in characteristics upon exposure to both electrons and heavier particles such as helium ions.

4.3.1 Electron Irradiation

Electron irradiation of these devices with energies in the order of a few keV will eventually desorb the hydrogen layer, as discussed in section 3.2. This has previously been demonstrated for $\sim$ 2 hour exposure using a ~ 3.5 keV electron sputtergun [41]. However, a layer of MoO_3 deposited at the surface may provide shielding to the hydrogen layer. Since the devices are believed to be more sensitive towards energies of this magnitude, the experiment is repeated under the same conditions, but for previously unexposed devices with an MoO_3 adsorbate. By irradiating inside a UHV chamber which holds a pressure of approximately $3 \cdot 10^{-10}$mbar, one can minimize the effect of energy loss and beam deflection due to possible interactions with other molecules. Also, by performing the irradiation in the same chamber as the PES measurements, it is possible to avoid the probability of contaminants affecting the results.

4.3.2 Helium Ion Irradiation

Sample 2 was exposed to 5 keV He^+ ions for $\sim$ 2hours in UHV. In order to estimate the dose rate and total dose, the drain current I_d from the sample holder was measured. The measurement is an implication of the number of ions implanted, as all excess charge will contribute to the current. The dose rate can be estimated as

$$\dot{D} = \frac{\overline{I_d(t)}}{eA}, \tag{32}$$

where e is the elementary charge and A is the cross-sectional area of the beam. The total dose after a time $T = 2$ hours is then calculated from

$$D = \frac{\int_0^T I_d(t)}{eA} \tag{33}$$

5 Results

5.1 SEM

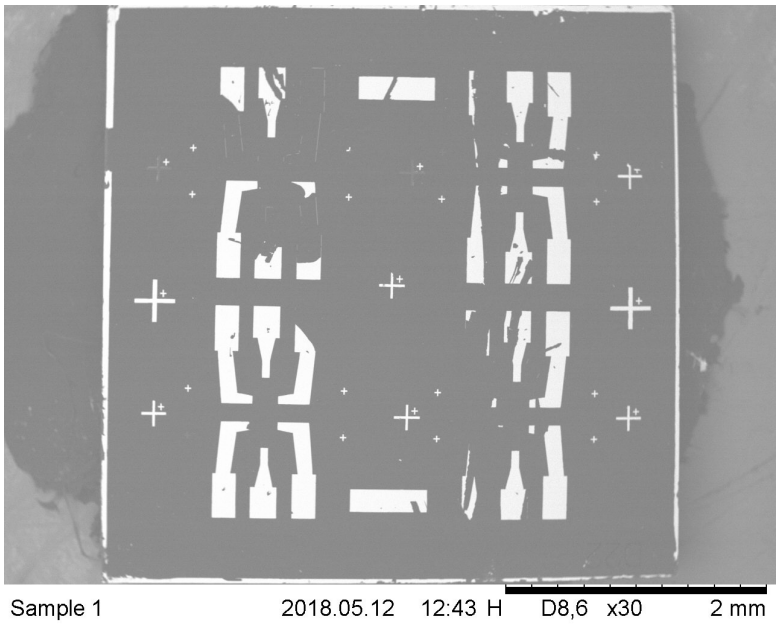

Figure 17: SEM image of sample 1. The lower-left device has the most intact contact pads, and will therefore be used for measurements.

The SEM image of sample 1 can be seen in Figure 17. Apart from the lower-left device, most of the contact pads has severe damage in vital regions near the hydrogen channel. This device, which is hereby referred to as *sample 1 device 1* (S1D1), is therefore used for the 4-point measurements.

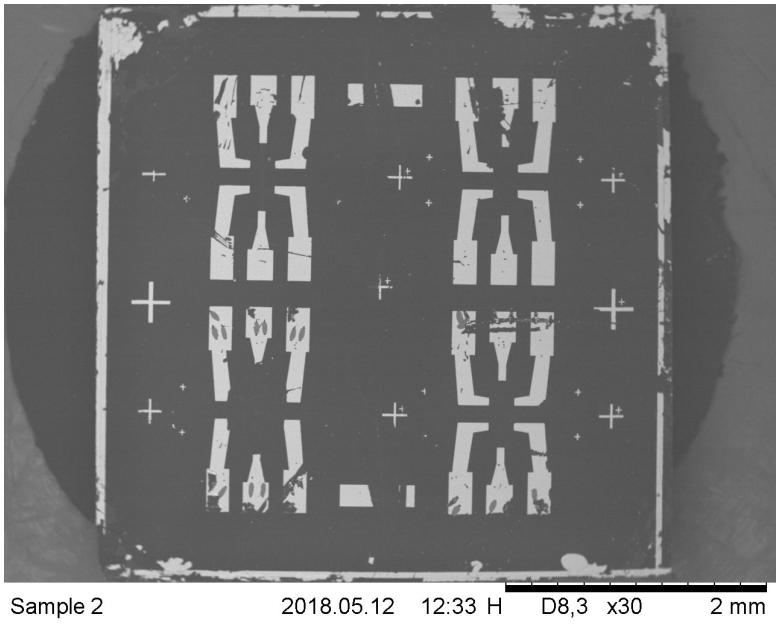

Figure 18: SEM image of sample 2. Both the upper-left and lower-right devices have fairly intact contact pads. The lower-right has a desorbed hydrogen channel from previous experiments, so the upper-left device will be used for measurements.

Figure 18 depicts the SEM image of the second sample. The upper-left and lower-right devices has contacts that are intact in the vital regions. However, the lower-right device has been irradiated with electrons in the

past, and thus do no longer have a conducting channel. For this reason, the upper-left device is chosen for 4-point measurements, and will hereafter be referred to as *sample 2 device 1* (S2D1).

5.2 MoO_3 Deposition

5.2.1 Thickness Estimation

After measuring the C1s level of the clean sample through XPS, MoO_3 was evaporated onto surface of sample 1 for ~ 10 min. The measured intensity after deposition is shown in Figure 19 along with the pre-deposition measurement.

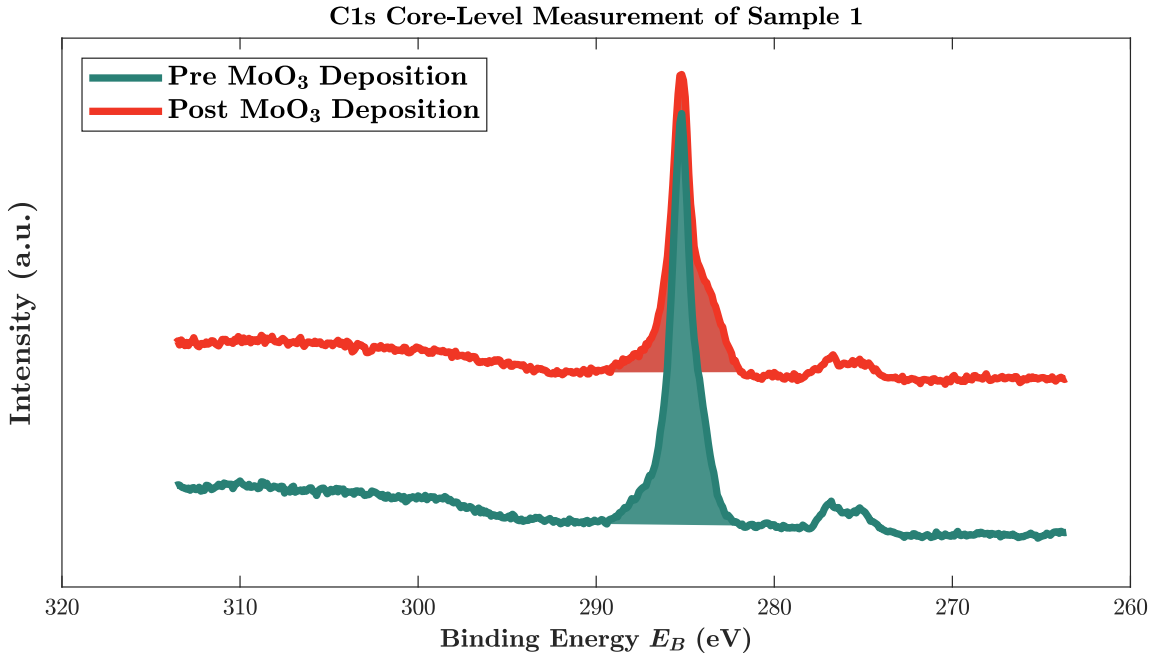

Figure 19: C1s peaks of sample 1, before and after MoO_3 deposition. The colored regions is the area used for thickness estimation for each peak.

The intensity peaks occurs at a kinetic energy ~ 968.4 eV, which corresponds to $\lambda_{MoO_3} = 19.6$ Å in Figure 9. The resulting MoO_3 layer thickness was calculated from equation 31, yielding a value of $t \approx 0.481$ nm. As for sample 2, MoO_3 was evaporated for ~ 22 min. The resulting change in intensity can be seen in Figure 20.

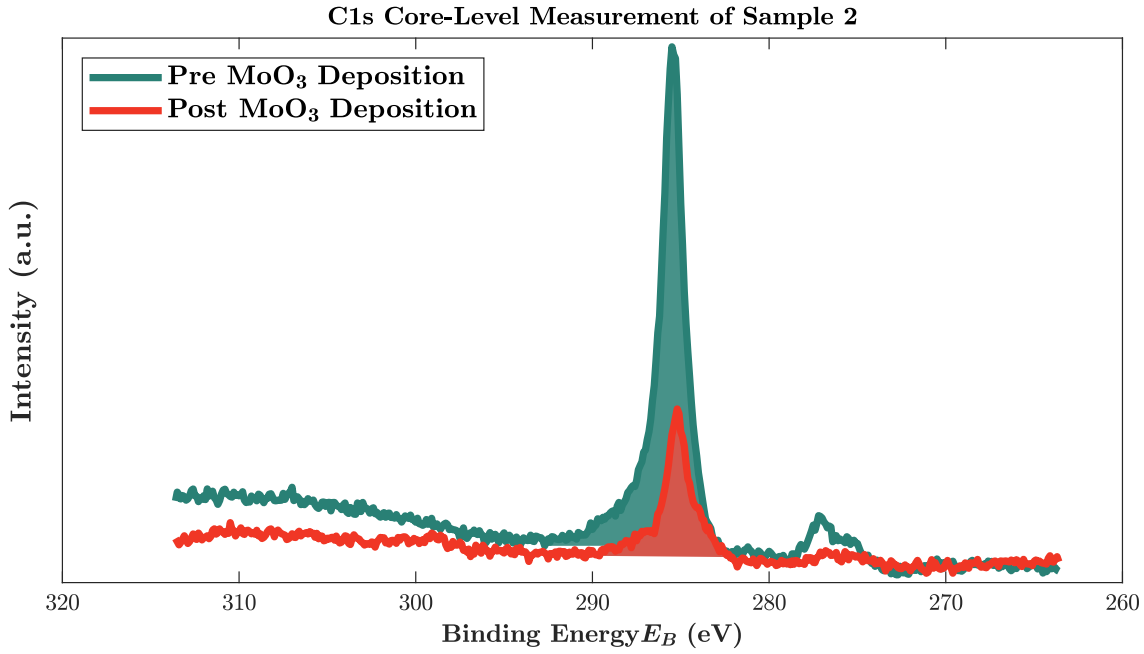

Figure 20: C1s peaks of sample 2, before and after MoO_3 deposition.

The thickness of the MoO_3 layer on sample 2 was estimated to $t \approx 2.314\,\text{nm}$.

5.2.2 Effect on Conductivity

In order to see how the MoO_3 layer affects the conductivity of the samples, 4-point measurements were performed at room temperature according to section 4.1.2. The obtained $I-V$ curves for S1D1 before and after deposition yields an increase in resistivity, as shown in Figures 21 and 22.

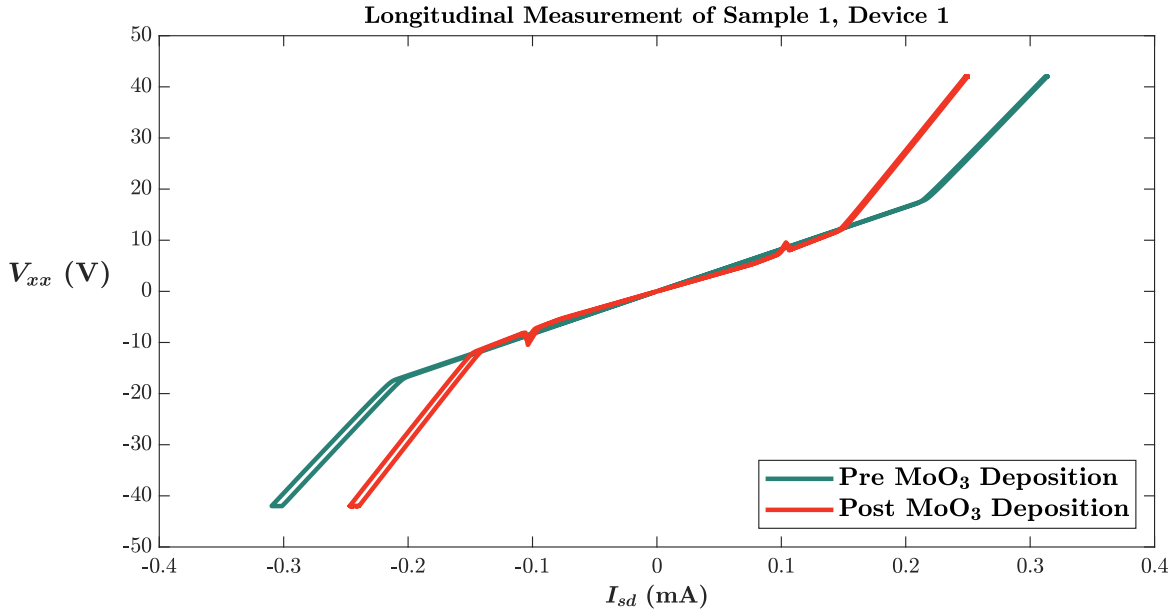

Figure 21: $I_{sd} - V_{xx}$ measurement of S1D1, showing an increased sheet resistivity after MoO_3 deposition.

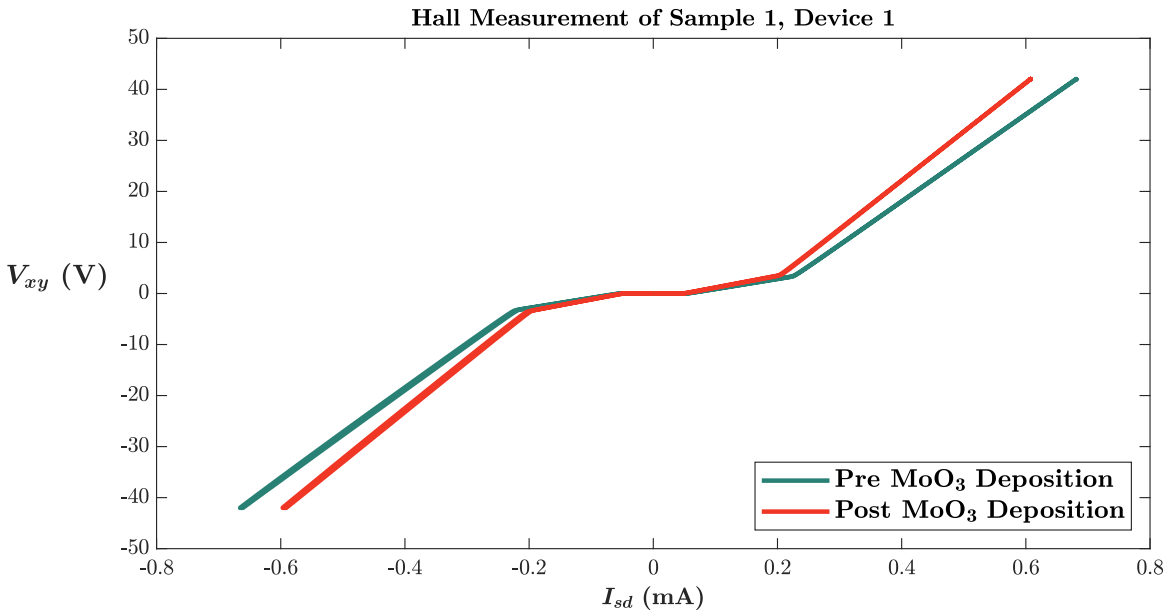

Figure 22: $I_{sd} - V_{xy}$ measurement of S1D1, showing an increased Hall resistivity after MoO_3 deposition.

The obtained electrical properties shown in Table 1 suggests that the 0.5 nm MoO_3 deposition results in a decrease in both sheet density and mobility, and thus also conductivity.

S1D1 Electrical Properties					
Condition	ρ_s ($\Omega\square^{-1}$)	ρ_H ($\Omega\square^{-1}$)	n_s (m^{-2})	μ ($m^2V^{-1}s^{-1}$)	σ_0 ($\square\Omega^{-1}$)
Pre dep.	$2.35 \cdot 10^4$	$3.68 \cdot 10^4$	$4.66 \cdot 10^{13}$	$5.68 \cdot 10^{-2}$	$4.25 \cdot 10^{-5}$
Post dep.	$2.93 \cdot 10^4$	$4.38 \cdot 10^4$	$3.92 \cdot 10^{13}$	5.43	$3.41 \cdot 10^{-5}$
Change	+25%	+19%	−16%	−4.4%	−20%

Table 1: Electrical properties of S1D1, before and after MoO_3 deposition. The performed measurements suggests a decrease in conductivity.

Similar measurements performed on S2D1 also yields increased resistivities, as seen in Figures 23 and 24.

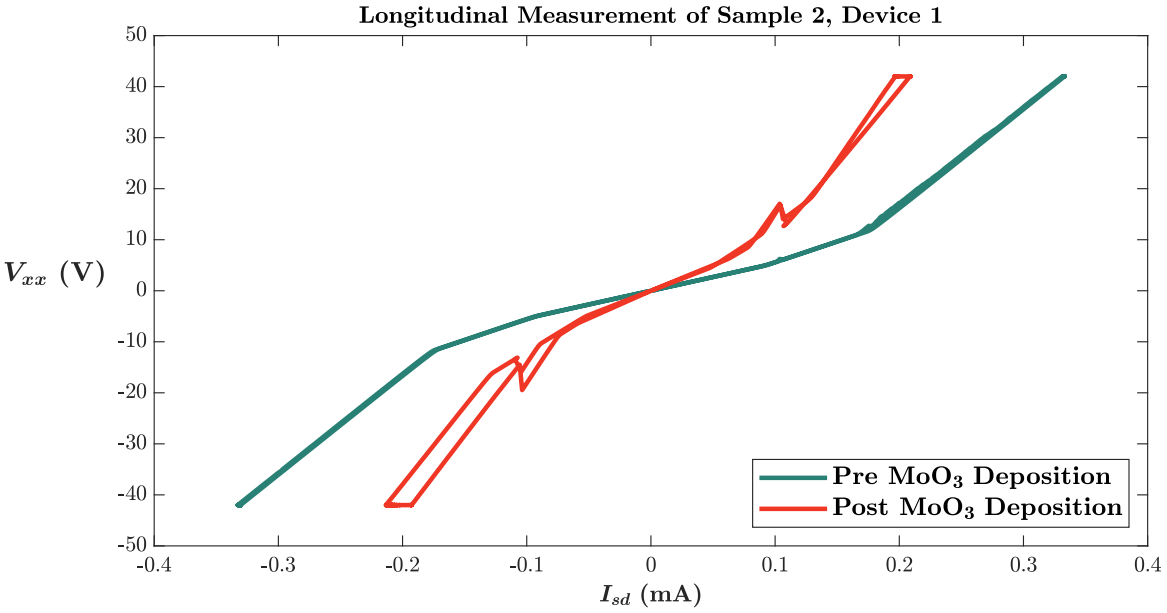

Figure 23: $I_{sd} - V_{xx}$ measurement of S2D1, showing an increased sheet resistivity after MoO_3 deposition.

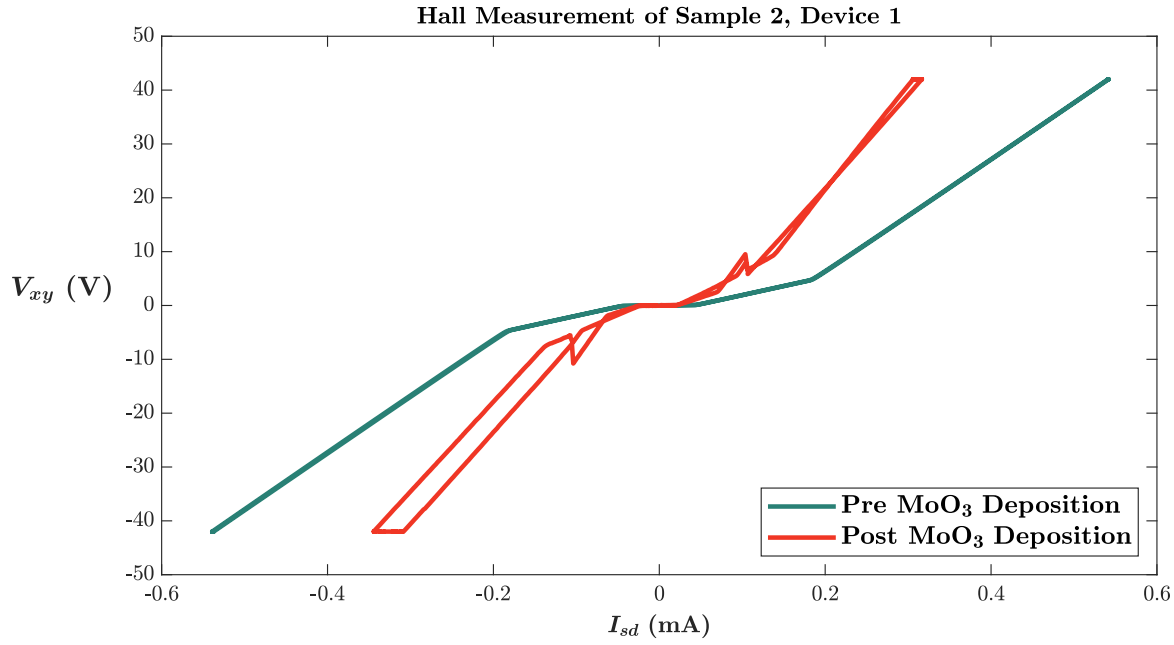

Figure 24: $I_{sd} - V_{xy}$ measurement of S2D1, showing an increased Hall resistivity after MoO_3 deposition.

The obtained electrical properties shown in Table 2 suggests that the 2.3 nm MoO_3 deposition results in an even more severe decrease in conductivity than for S1D1.

S2D1 Electrical Properties					
Condition	ρ_s ($\Omega\square^{-1}$)	ρ_H ($\Omega\square^{-1}$)	n_s (m^{-2})	μ ($\mathrm{m}^2\mathrm{V}^{-1}\mathrm{s}^{-1}$)	σ_0 ($\square\Omega^{-1}$)
Pre dep.	$2.11 \cdot 10^4$	$6.77 \cdot 10^4$	$2.54 \cdot 10^{13}$	11.7	$4.74 \cdot 10^{-5}$
Post dep.	$3.78 \cdot 10^4$	$1.10 \cdot 10^5$	$1.57 \cdot 10^{13}$	10.5	$2.65 \cdot 10^{-5}$
Change	+79%	+63%	−38%	−10%	−44%

Table 2: Electrical properties of S1D1, before and after MoO_3 deposition. The performed measurements suggests a strong decrease in conductivity.

5.3 Electron Irradiation

Assuming $A \sim 1\,\mathrm{cm}^2$ for the beam, the dose rate is estimated to $6.24 \cdot 10^{13}$ electrons/cm^2/s, with a total dose of $4.49 \cdot 10^{17}$ electrons/cm^2 based on the average measured drain current of $10\,\mu$A. The UPS measurements for one of the positions before and after ~ 2 hours exposure to 3.5 keV electrons is shown in Figures 25 and 26 for the low- and high-energy regime respectively.

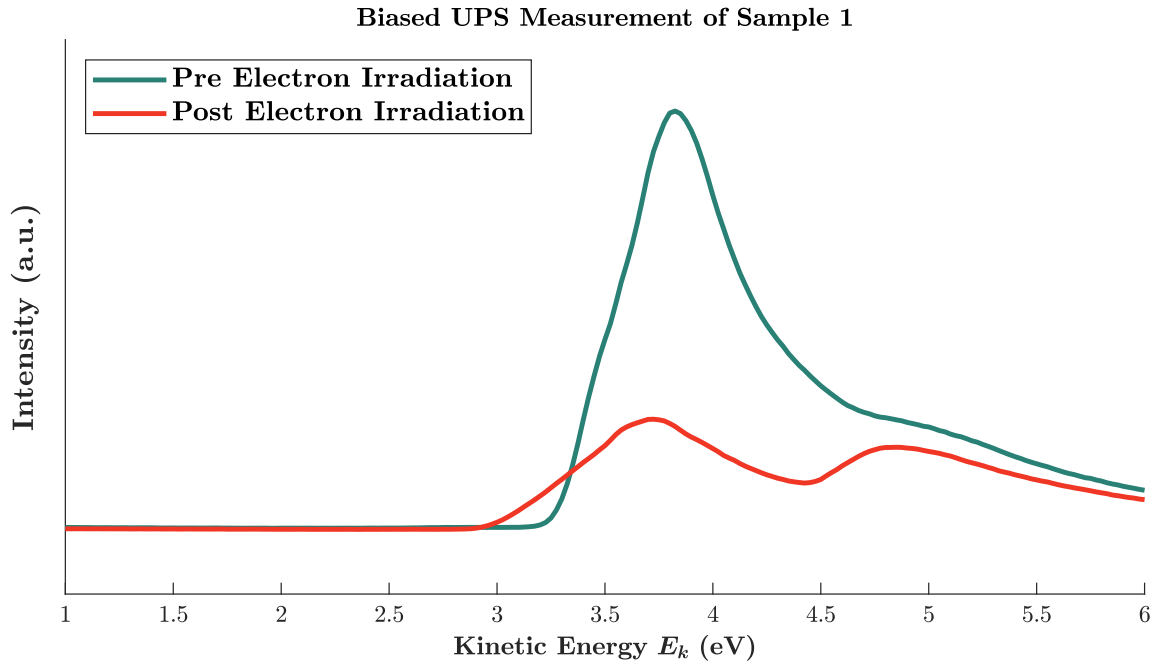

Figure 25: Biased UPS measurement of sample 1, position 3 before and after electron irradiation. $E_{k,min}^{meas}$ is the cutoff where the intensity of detected electrons suddenly drops to zero around 3 eV.

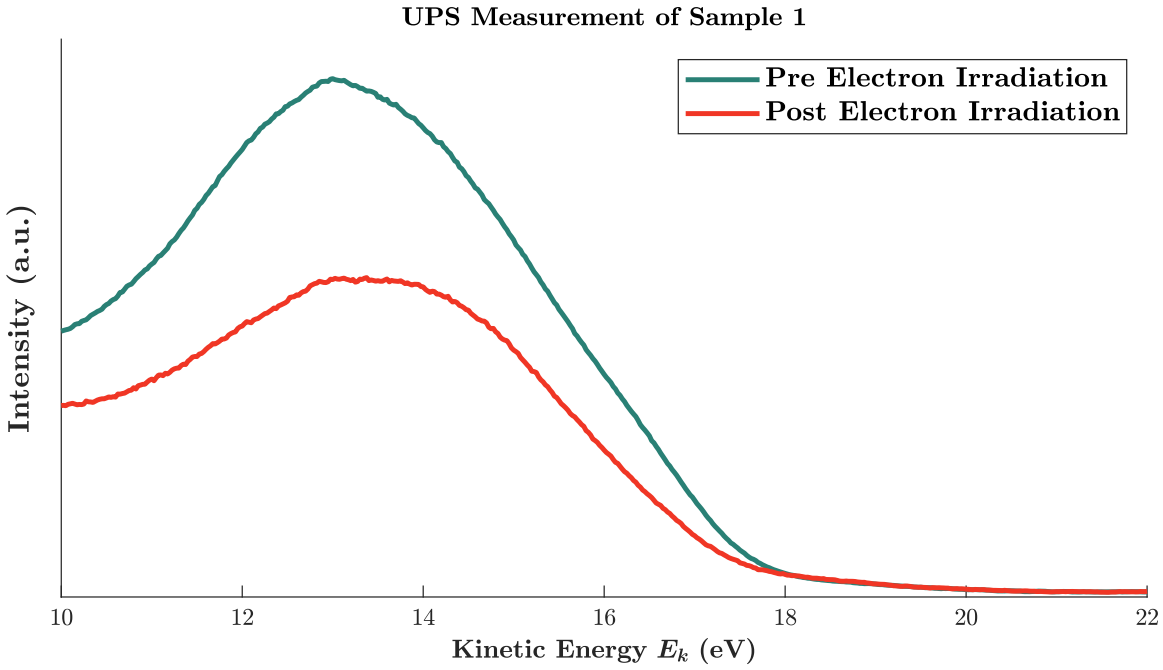

Figure 26: UPS measurement of sample 1, position 3 before and after electron irradiation. $E_{k,max}^{meas}$ is the cut-off where the intensity of detected electrons suddenly drops to zero around 18 eV.

The XPS meaurement for sample 1 is shown in Figure 27.

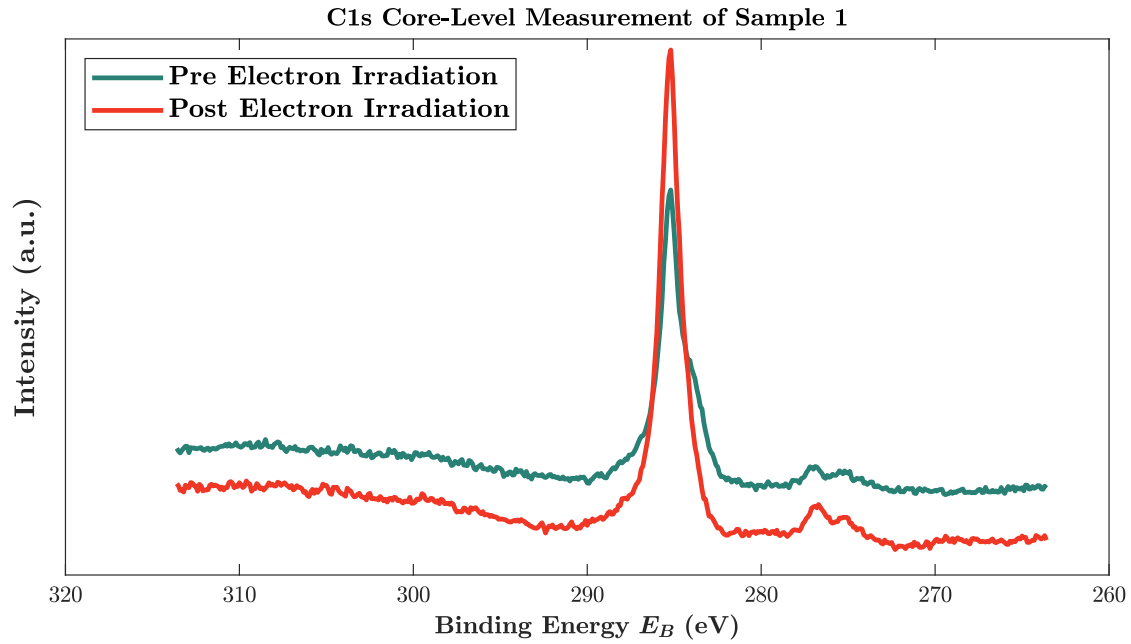

Figure 27: XPS spectrum of sample 1, before and after electron irradiation. The C1s binding energy is where the intensity peaks, around 285 eV.

Based on the XPS analysis in Figure 27, the C1s binding energy is found to be $E_B = 285.2$ eV relative to the

Fermi level, corresponding to $E_F - E_V = 1.3\,\text{eV}$.
The the work function, electron affinity and ionization energy of the sample are calculated from the width of the UPS spectrum and the binding energy obtained from XPS. The results are shown in Table 3.

Sample 1 Surface Properties						
Position	**Condition**	$E^{meas}_{k,max}$ **(eV)**	$E^{meas}_{k,min}$ **(eV)**	Φ_S **(eV)**	χ **(eV)**	I **(eV)**
1	**Pre-irr.**	17.380	2.325	6.145	1.945	7.445
	Post-irr.	17.150	2.350	6.400	2.200	7.700
	Change	−1.3%	+1.1%	+4.2%	+13%	+3.4%
2	**Pre-irr.**	17.700	2.550	6.050	1.850	7.350
	Post-irr.	17.350	2.250	6.100	1.900	7.400
	Change	−2.0%	−12%	+0.8%	+2.7%	+0.7%
3	**Pre irr.**	17.700	3.275	6.775	2.575	8.075
	Post irr.	17.480	3.000	6.720	2.520	8.020
	Change	−1.2%	−8.4%	−0.8%	−2.1%	−0.7%

Table 3: Surface properties of sample 1, before and after electron irradiation.

The I-V measurements in Figures 28 and 29 shows a clear increase in resistivities for S1D1 after exposure.

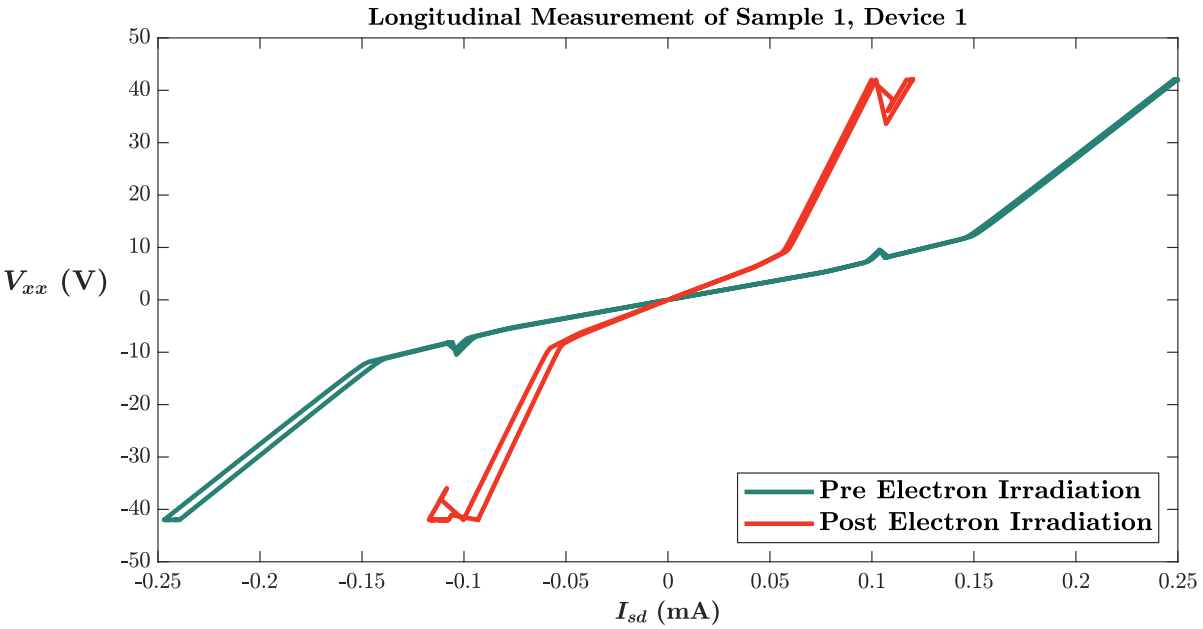

Figure 28: $I_{sd} - V_{xx}$ measurement of S1D1, showing an increased sheet resistivity after electron irradiation.

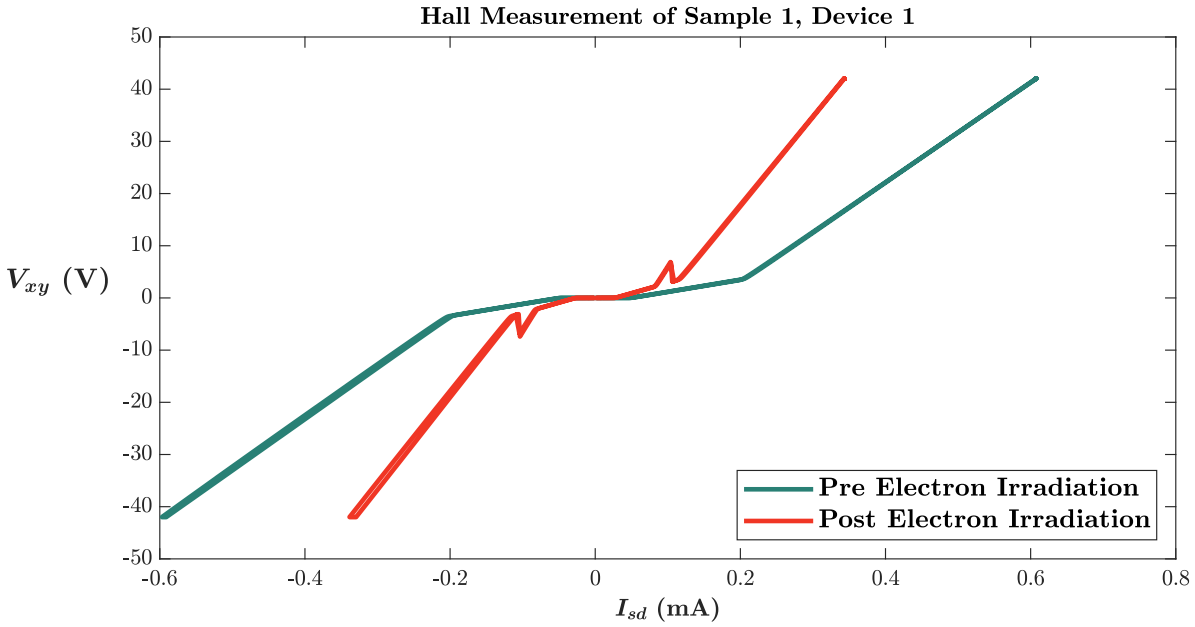

Figure 29: $I_{sd} - V_{xy}$ measurement of S1D1, showing an increased Hall resistivity after electron irradiation.

The obtained electrical properties shown in Table 4 suggests that the electron exposure triggers a strong decrease in conductivity.

S1D1 Electrical Properties					
Condition	ρ_s ($\Omega\square^{-1}$)	ρ_H ($\Omega\square^{-1}$)	n_s (m^{-2})	μ ($\mathrm{m}^2\mathrm{V}^{-1}\mathrm{s}^{-1}$)	σ_0 ($\square\Omega^{-1}$)
Pre irr.	$2.93 \cdot 10^4$	$4.38 \cdot 10^4$	$3.93 \cdot 10^{13}$	5.43	$3.41 \cdot 10^{-5}$
Post irr.	$6.90 \cdot 10^4$	$9.77 \cdot 10^4$	$1.76 \cdot 10^{13}$	5.15	$1.45 \cdot 10^{-5}$
Change	+136%	+123%	−55%	−5.2%	−58%

Table 4: Electrical properties of D1D1, before and after electron irradiation. The performed measurements suggests a strong decrease in conductivity.

5.4 Helium Ion Irradiation

Assuming a cross-sectional area of $A \sim 1\ \mathrm{cm}^2$ for the beam, the total dose and dose rate was estimated to $7.39 \cdot 10^{16}$ ions/cm^2 and $9.67 \cdot 10^{12}$ ions/cm^{2}s respectively. After exposing sample 2 to 5 keV He^+ ions for ~ 2 hours, a clear change in color was observed as seen in Figure 30.

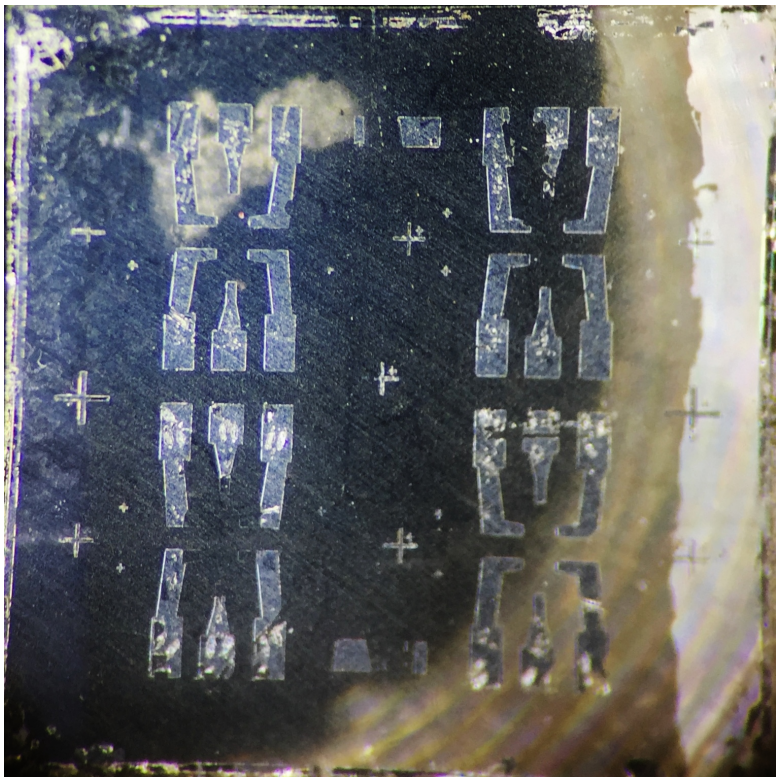

Figure 30: Photo of sample 2 after helium ion dosing. Apart from the edges, the entire sample surface became darker after exposure. This is evident by looking at the right edge of the photo, showing the border between the transparent diamond and the dark part.

The UPS measurements for one of the positions is shown in Figures 25 and 26 for the low- and high-energy regime respectively.

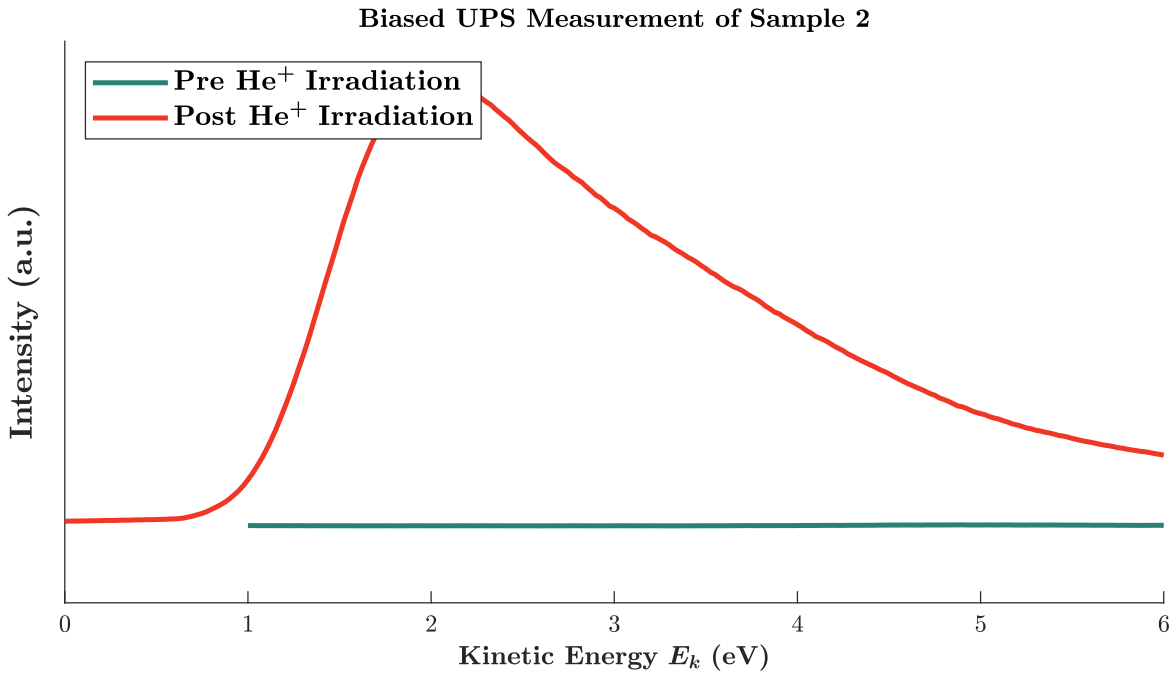

Figure 31: UPS measurement of sample 2 position 3, before and after He^+ irradiation. $E_{k,min}^{meas}$ is the cutoff where the intensity of detected electrons suddenly drops to zero around 1 eV.

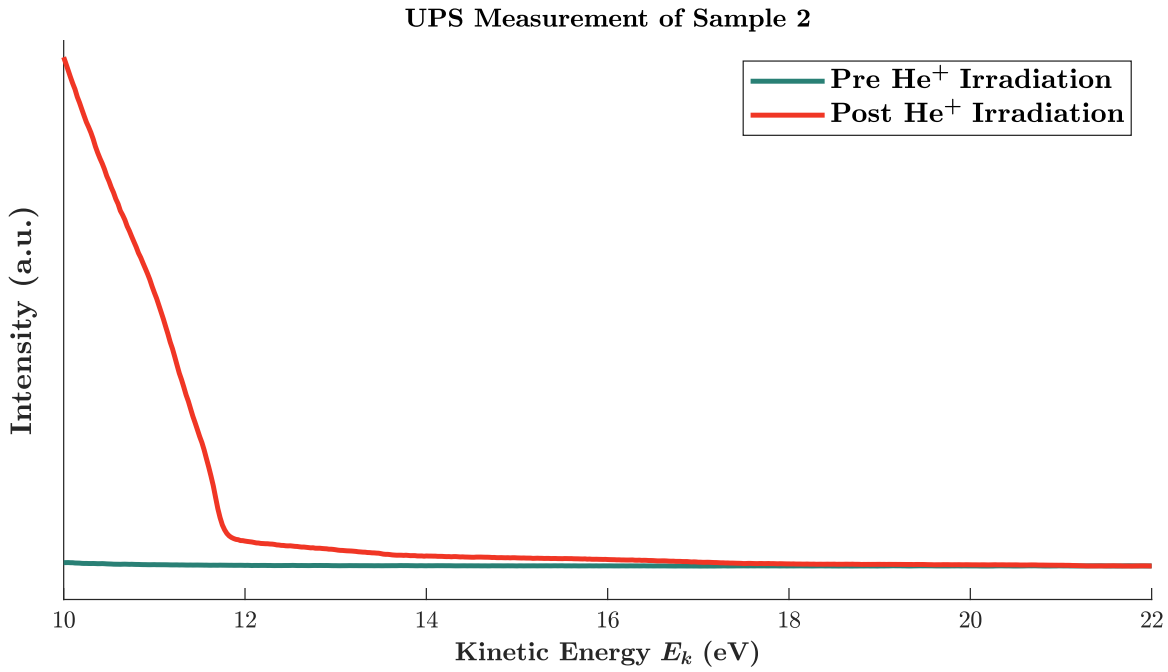

Figure 32: UPS measurement of sample 2 position 3, before and after He^+ irradiation. $E_{k,max}^{meas}$ is the cutoff where the intensity of detected electrons suddenly drops to zero around 12 eV.

The XPS measurement for sample 2 is shown in Figure 33.

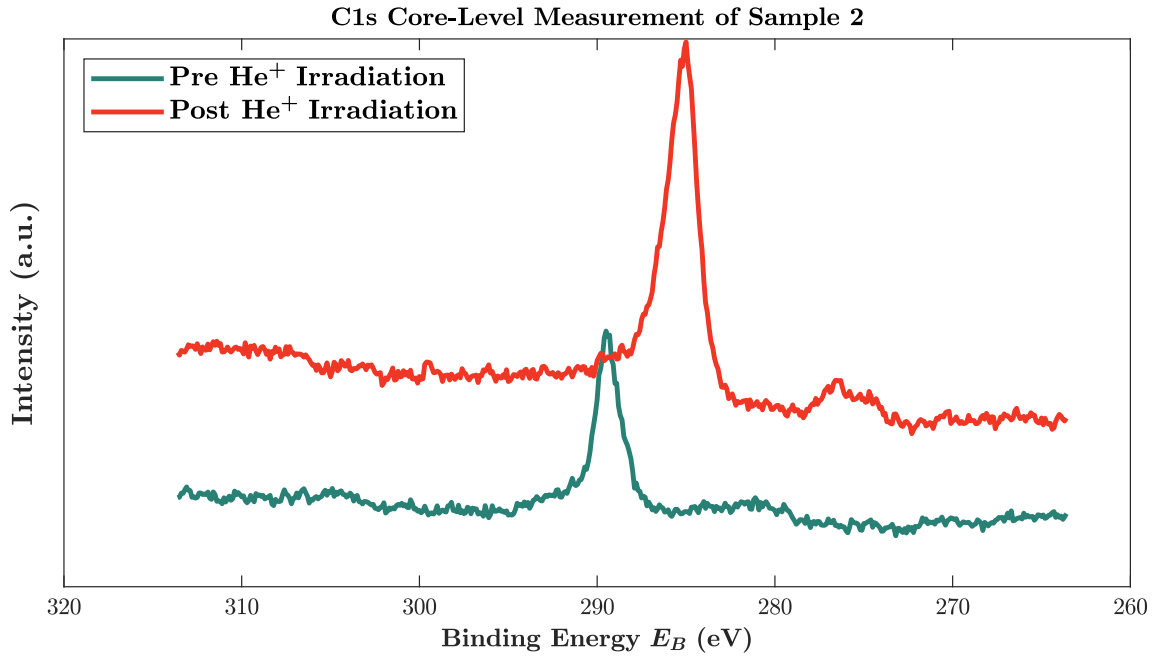

Figure 33: XPS spectrum of sample 2, before and after He^+ irradiation. The C1s binding energy is where the intensity peaks which is around 290 eV before irradiation, and shifted to about 285 eV after irradiation.

Based on the XPS analysis in Figure 33, the C1s binding energy is shifted from $E_B = 289.5$ eV relative to the Fermi level to 285.0 eV after helium ion dosing. This corresponds to i shift in the position of the valence band

maximum from $E_F - E_V = 5.9\,\text{eV}$ to $E_F - E_V = 1.1\,\text{eV}$. The the work function, electron affinity and ionization energy of the sample are calculated from the width of the UPS spectrum and the binding energy obtained from XPS. The results are shown in Table 5.

Sample 2 Surface Properties						
Position	**Condition**	$E_{k,max}^{meas}$ **(eV)**	$E_{k,min}^{meas}$ **(eV)**	Φ_S **(eV)**	χ **(eV)**	I **(eV)**
1	**Pre-irr.**	15.030	3.000	9.170	9.570	15.070
	Post-irr.	11.900	0.700	10.000	5.600	11.100
	Change	−21%	−77%	+9.1%	−42%	−26%
2	**Pre-irr.**	13.530	3.175	10.845	11.245	16.745
	Post-irr.	11.900	0.675	9.975	5.575	11.075
	Change	−12%	−79%	−8.0%	−50%	−34%
3	**Pre irr.**	11.570	3.525	13.155	13.555	19.055
	Post irr.	11.930	1.025	10.295	5.895	11.395
	Change	+3.1%	−71%	−22%	−57%	−40%

Table 5: Surface properties of sample 2, before and after helium ion irradiation.

5.4.1 Raman Analysis

The collected Raman spectra containing characteristic diamond shifts *before* helium ion dosing are shown in Figure 34. The location of these spectra on the sample can be seen in Figure 35, where it is evident that many of the spectra contains neither diamond or graphite shifts.

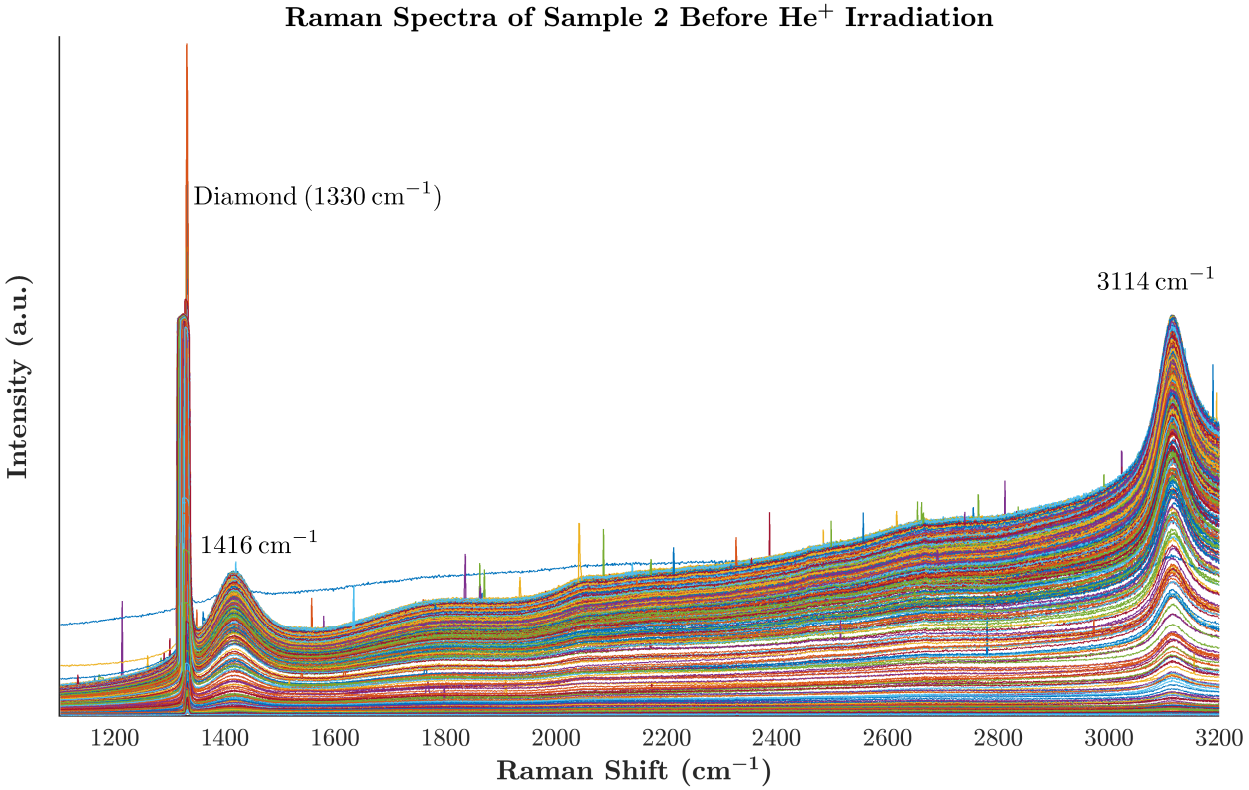

Figure 34: Raman spectrum showing the diamond peaks ($\approx 1330\,\text{cm}^{-1}$ in sample 2 before helium dosing. There are also two other distinct peaks present around $1416\,\text{cm}^{-1}$ and $3114\,\text{cm}^{-1}$.

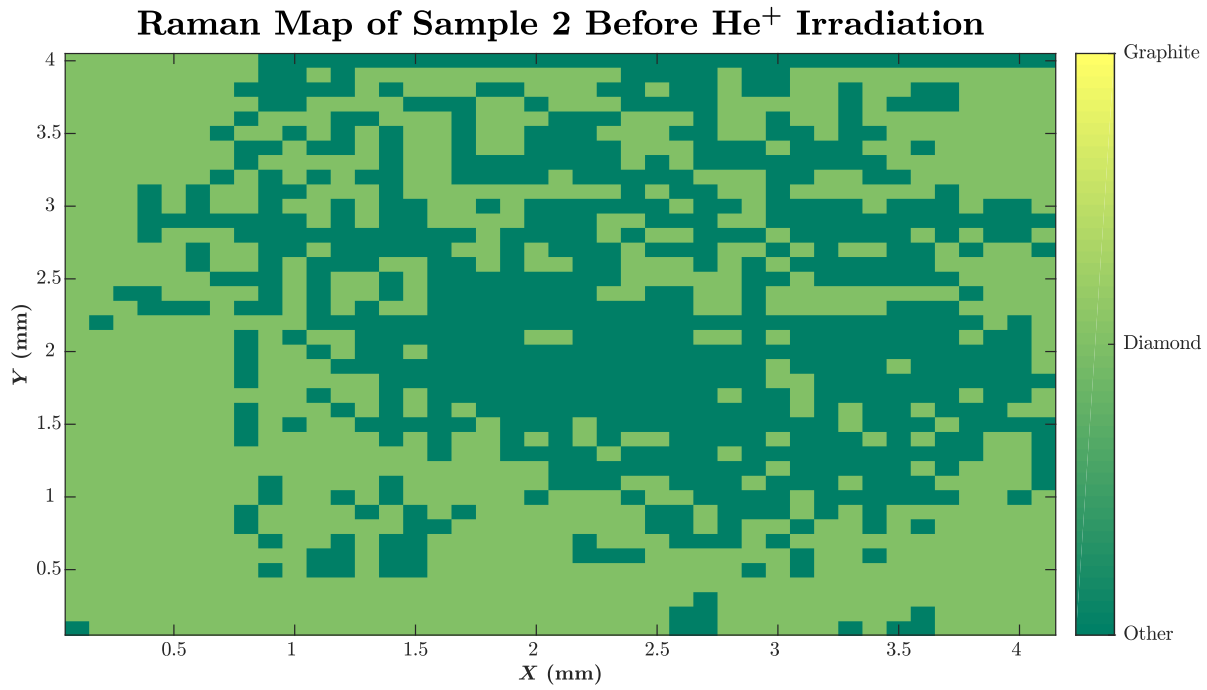

Figure 35: Raman map of sample 2 before helium ion dosing.

The spectra containing diamond shifts *after* helium ion dosing are shown in Figure 36.

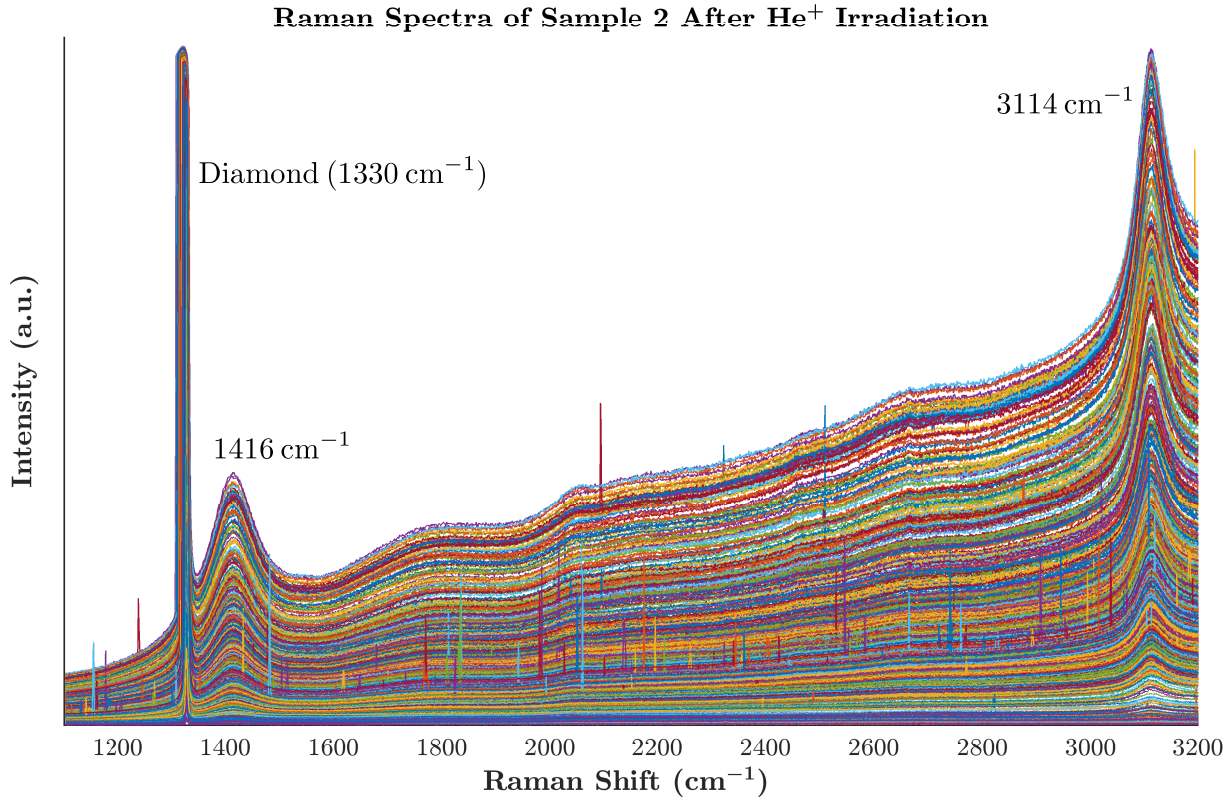

Figure 36: Raman spectrum showing the diamond peak in sample 2 after helium dosing. There are also two other distinct peaks present around 1416 cm^{-1} and 3114 cm^{-1}.

From the map scan, a single spectrum containing a 2D graphite shift was also detected, as seen in Figure 37. This location of this possible graphitic region is indicated in the map in Figure 38.

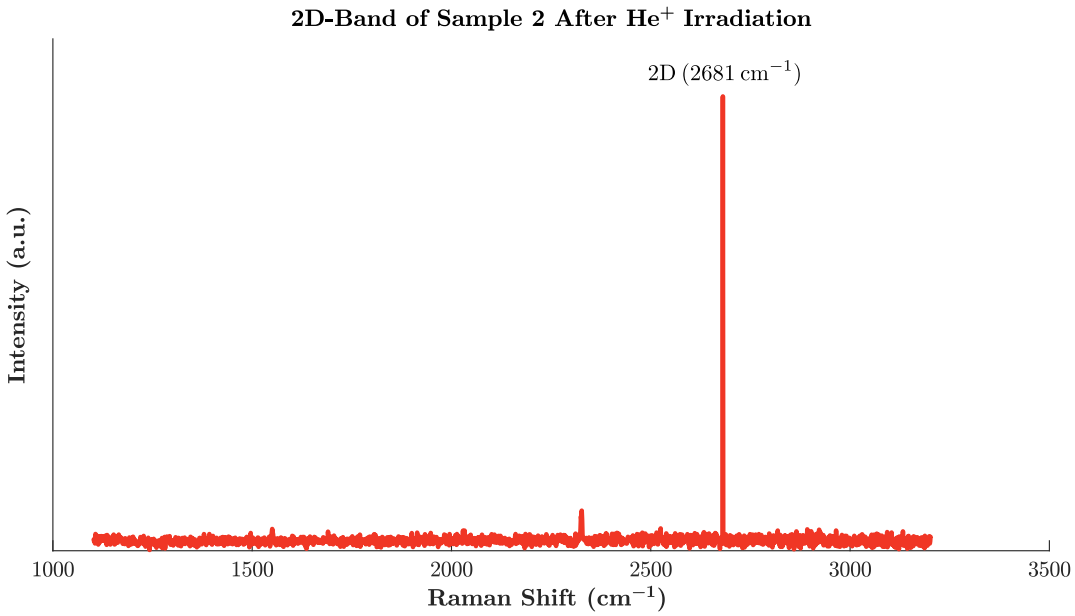

Figure 37: Raman spectrum showing the 2D graphite peak in sample 2, after helium dosing.

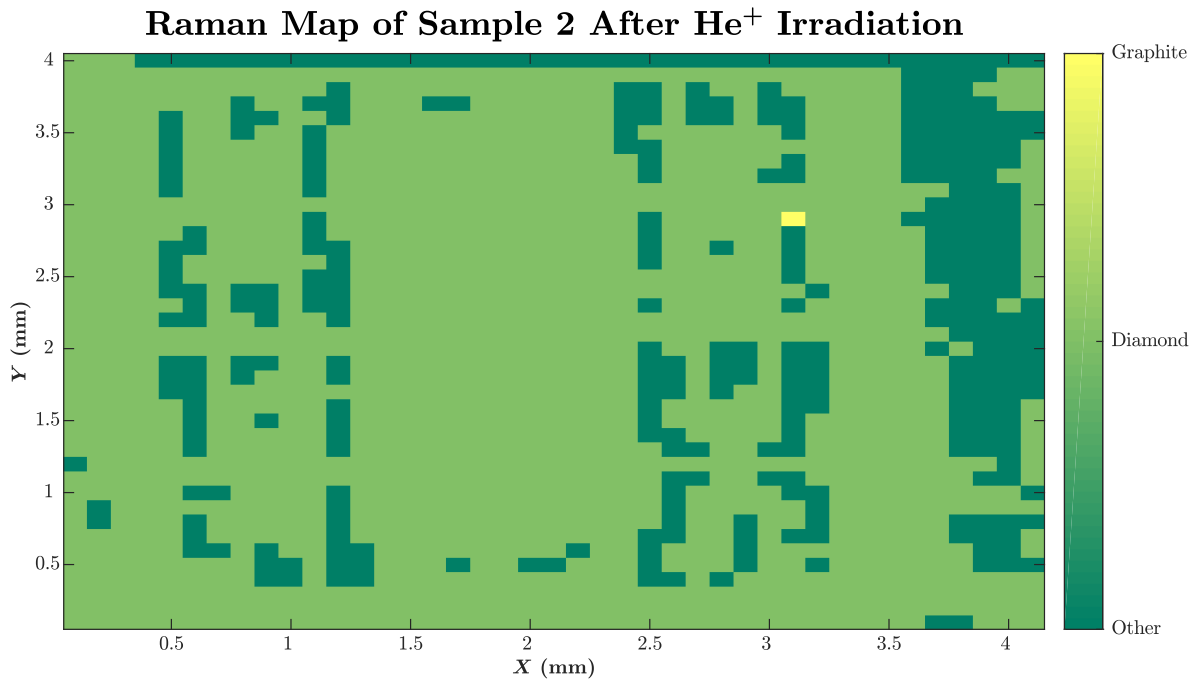

Figure 38: Raman map of sample 2 after helium dosing, indicating graphitized regions.

5.4.2 Electrical Properties

The *I-V* measurements in Figures 39 and 40 shows a clear increase in resistivities for S2D1 after exposure.

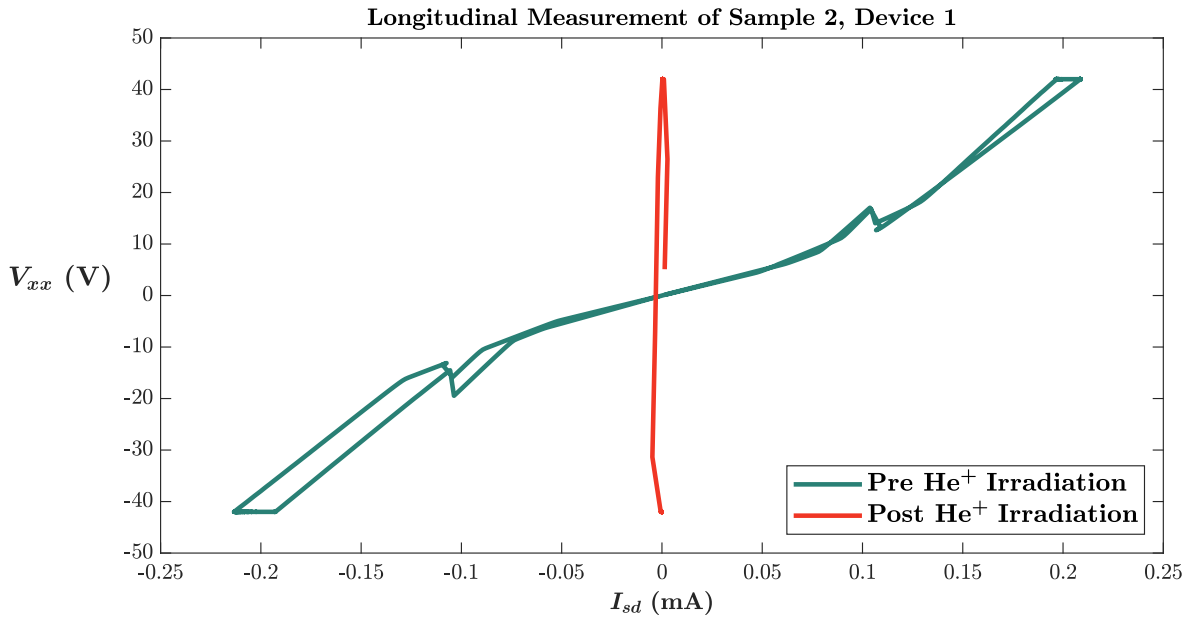

Figure 39: $I_{sd} - V_{xx}$ measurement of S2D1, showing an increased sheet resistivity after helium ion irradiation.

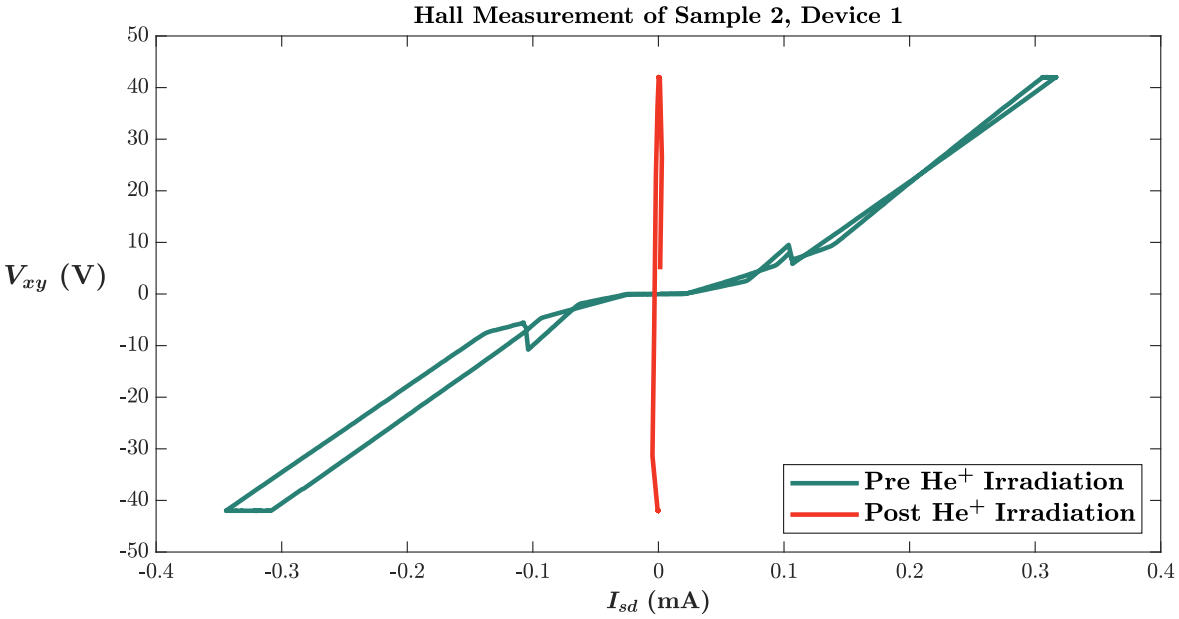

Figure 40: $I_{sd} - V_{xy}$ measurement of S2D1, showing an increased Hall resistivity after helium ion irradiation.

The obtained electrical properties shown in Table 6 suggests that the helium ion exposure triggers a strong decrease in conductivity.

S2D1 Electrical Properties					
Condition	ρ_s ($\Omega\square^{-1}$)	ρ_H ($\Omega\square^{-1}$)	n_s (m^{-2})	μ ($\mathrm{m}^2\mathrm{V}^{-1}\mathrm{s}^{-1}$)	σ_0 ($\square\Omega^{-1}$)
Pre irr.	$3.78 \cdot 10^4$	$1.10 \cdot 10^5$	$1.57 \cdot 10^{13}$	10.5	$2.65 \cdot 10^{-5}$
Post irr.	$5.00 \cdot 10^7$	$1.82 \cdot 10^8$	$9.44 \cdot 10^9$	13.2	$2.00 \cdot 10^{-8}$
Change	+132175 %	+165355 %	−100 %	+26 %	−100 %

Table 6: Electrical properties of S2D1, before and after helium ion dosing. The values indicate a clear drop in conductivity after helium ion exposure.

For comparison, I-V measurements was also performed on one of the other devices on the helium dosed sample. The hydrogen channel on this device had previously been desorbed, which is indicated in Figures 41 and 42. The measurements actually indicate a strong *decrease* in resistivity for this device.

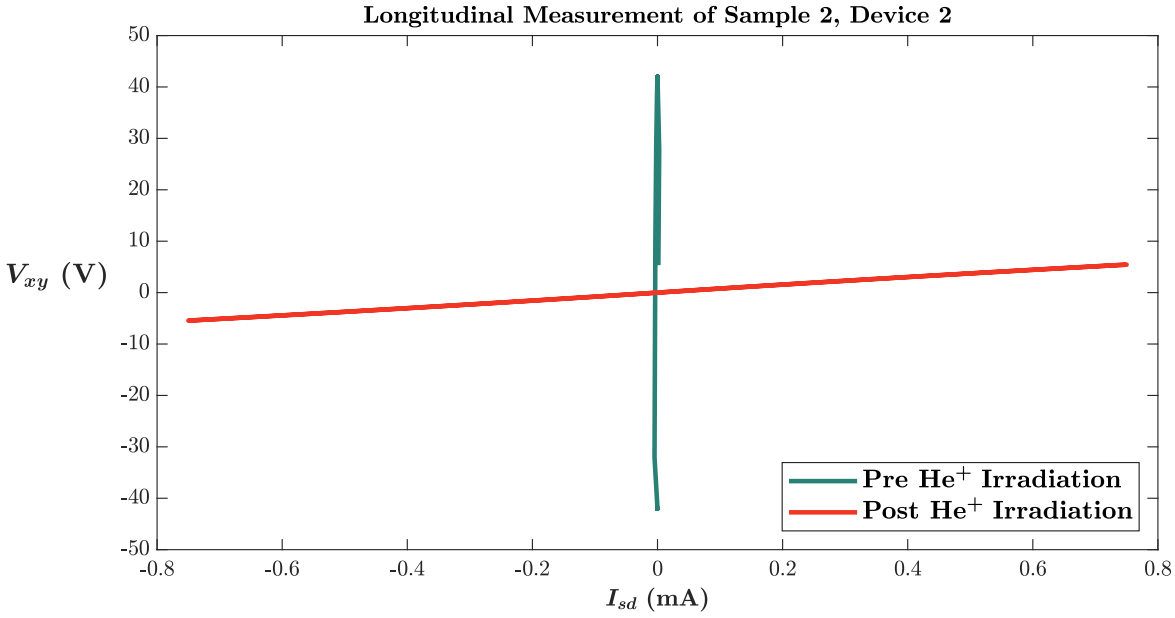

Figure 41: $I_{sd} - V_{xx}$ measurement of S2D2, indicating a clear drop in sheet resistivity after helium ion exposure.

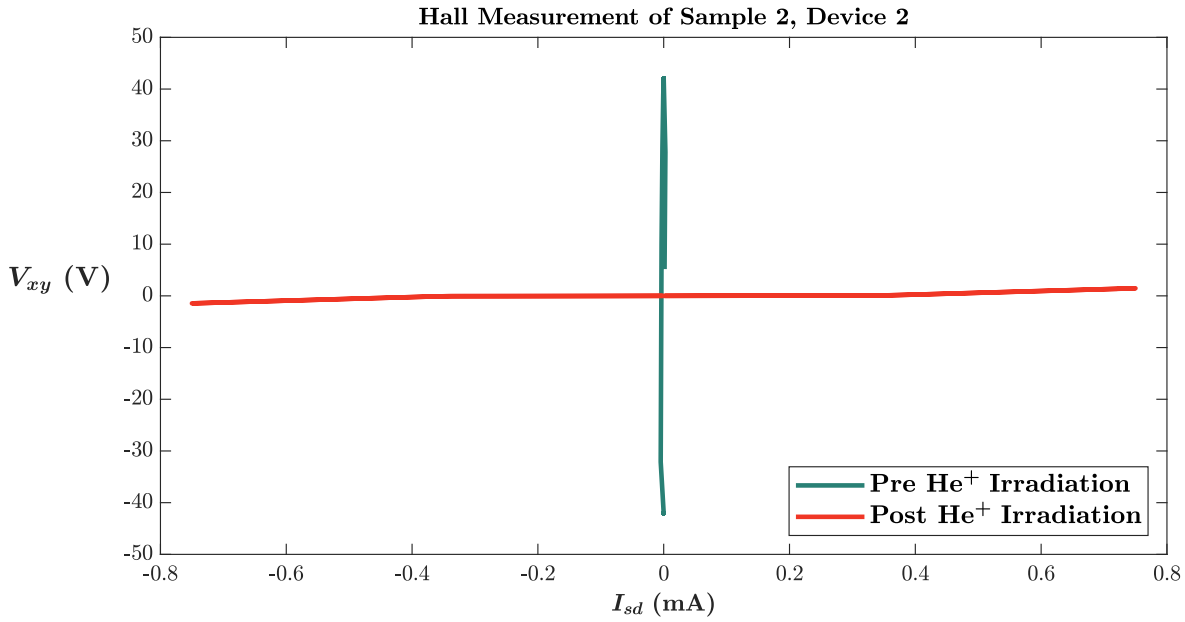

Figure 42: $I_{sd} - V_{xy}$ measurement of S2D2, indicating a clear drop in Hall resistivity after helium ion exposure.

The obtained electrical properties for S2D2 shown in Table 6 suggests that the helium ion exposure triggers a strong *increase* in conductivity.

Sample 2, Device 2 Electrical Properties					
Condition	ρ_s ($\Omega\square^{-1}$)	ρ_H ($\Omega\square^{-1}$)	n_s (m^{-2})	μ ($m^2V^{-1}s^{-1}$)	σ_0 ($\square\Omega^{-1}$)
Pre irr.	$-1.39 \cdot 10^6$	$-7.71 \cdot 10^7$	$-2.23 \cdot 10^{10}$	202	$-7.20 \cdot 10^{-7}$
Post irr.	$1.52 \cdot 10^3$	$8.04 \cdot 10^2$	$2.14 \cdot 10^{15}$	1.92	$6.57 \cdot 10^{-4}$
Change	-100 %	-100 %	$+9.6 \cdot 10^6$ %	-99 %	$+91350$ %

Table 7: Electrical properties of S2D2, before and after helium ion dosing. The negative resistivity values prior to exposure originates from measurement uncertainties in the SMU. The change in conductivity thus indicate that the device has changed characteristics from insulating to conductive.

6 Discussion

6.1 Interpretation of Results

6.1.1 MoO_3 Deposition

The decrease in conductivity upon MoO_3 deposition presented in section 5.2 is somewhat surprising, considering the number of studies stating the opposite. Kalish *et al.* found that a certain thickness of MoO_3 is required in order for it to improve sheet density compared to H_2O [11]. This is illustrated in Figure 43.

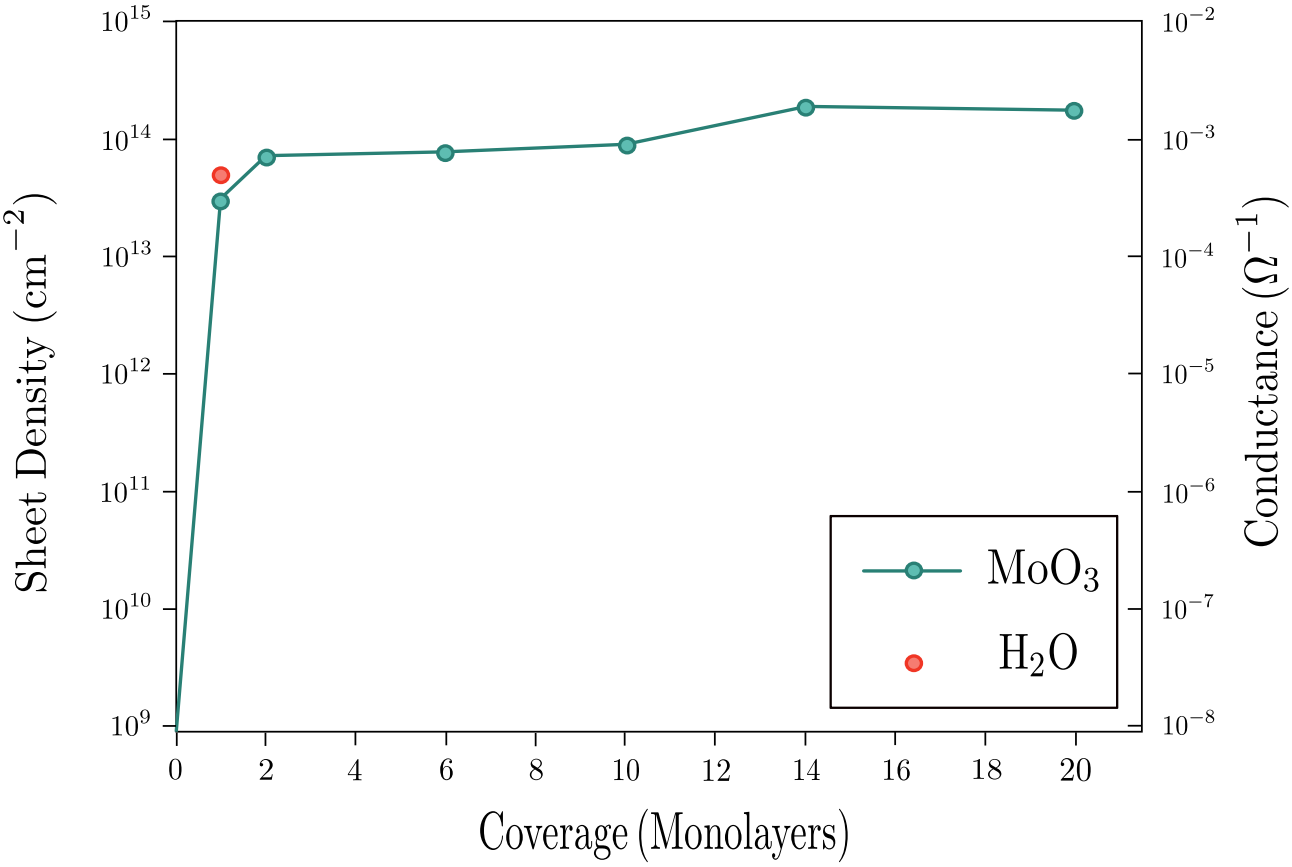

Figure 43: Sheet density dependence on MoO_3 thickness. After a deposition of ~ 2 monolayers (≈ 1.6 nm), a further increase in thickness does not affect the density significantly. - Illustration adapted from reference [11].

A monolayer of MoO_3 is ~ 0.8 nm thick [42]. This suggests that the thickness of the deposited layer should be ≥ 1.6 nm in order to obtain superior electrical characteristics. This may explain the decrease in conductivity for sample 1 which had a MoO_3 layer of only ~ 0.5 nm. However, sample 2 also obtained a lower conductivity after ~ 2.3 nm MoO_3 deposition. The reason for this is not known, but it might be due to contact issues as the MoO_3 was deposited on the whole sample and not just on the hydrogen channel. Another possible reason may be that the MoO_3 was not evenly distributed across the surface.

6.1.2 Electron Irradiation

The decrease in conductivity seen in Table 4 would suggest partly desorption of the hydrogen layer However, there is still a notable sheet density. Previously obtained results, where a similar device *without* MoO_3 was irradiated under the same conditions, have shown that this exposure would lead to complete desorption [41]. It is thus likely that the MoO_3 may have provided some shielding of the hydrogen channel. The reduction of the MoO_3 thickness based on Figure 27 is ≈ 0.765 nm. As the initial thickness was estimated to ≈ 0.481 nm, this may indicate that other surface species might have come off during exposure, which may be palladium hydrogen, oxygen or contaminants. It is therefore likely that the hydrogen would be completely desorbed if the exposure time was longer. The work function measurements in Table 3 before exposure seems to be slightly higher than the values found by Russel *et al.*, which states that $\Phi \approx 5.8$ eV could be expected for hydrogen terminated diamond with a ~ 0.5 nm MoO_3 layer [12]. As it is not known *exactly* where on the sample the different positions for photoemission are located, there is a probability that these measurements were taken from oxygen-terminated regions or across the palladium contacts. This may explain the offset from the expected values. A PEA is expected after MoO_3 deposition, but the same argument applies as for the work function, namely that the origin of the magnitude of the electron affinity is ambiguous due to the various surface materials present.

6.1.3 Helium Ion Irradiation

The change of color seen in Figure 30 is an indication of graphitization. This is also supported by the presence of the Raman graphite band in Figure 37. However, the fact that there are no G band present may indicate that there is a thin layer of *graphene* that has been created, as the 2D band is much more intense than the G band in graphene compared to graphite [40]. The fact that there is only one spectrum indicating graphitization may

originate from contamination, errors in the experimental procedure and the data processing. This hypothesis is supported by Figure 35, where there are several regions that does not contain a diamond shift even though that would be expected. The same issue occurs after helium dosing as seen in Figure 38. All though the middle region now has diamond shifts, except for the regions where the contacts are located, there is still a large area near the edge which should yield diamond shifts. Apart from the characteristic diamond bands in Figures 34 and 36, there are two distinct peaks at $1416\,\mathrm{cm}^{-1}$ and $3114\,\mathrm{cm}^{-1}$ which may be indicative of CH_2 bending and CH_2 stretching respectively [43][44]. However, the exact origin of these vibrational modes have not been investigated. The *I-V* measurements are also somewhat complicated to interpret as one device yields a strong decrease in conductivity (Table 6) while another device, which was initially insulating, has become highly conductive upon the same exposure (Table 7). The reduction of the MoO_3 thickness based on Figure 27 is $\approx 1.760\,\mathrm{nm}$ from the initial $\approx 2.314\,\mathrm{nm}$. This is most likely due to ISD effects, causing MoO_3 to come off. This decrease in MoO_3 thickness may explain the decrease in conductivity for S2D1, in accordance with the discussion in section 6.1.1. As for the significant *increase* in conductivity obtained for S2D2, one possible explanation is that the ion beam was aimed closer to this device, causing local graphitization close to the surface in this region, and desorption in the region around S2D1. Whether or not this is responsible for the change in electrical properties depends on the exact region and *depth* at which graphitization have occurred. Due to the mentioned shortcomings in the Raman analysis, this cannot be manifested. The change in color suggests that the whole sample was graphitized, but the depth of possible graphitized regions is not known. Another possible explanation for the increase in conductivity is that the beam was actually aimed closer to S2D1, causing fragments of the palladium contacts to sputter, and eventually cover the region around S2D2 with conductive metal particles. Another surprising result is the C1s binding energy shift in Figure 33. The peak at $\approx 289.5\,\mathrm{eV}$ *prior* to ion bombardment is indicative of C=O bonds which is not consistent with the characteristic C−C bond energy at $\approx 285\,\mathrm{eV}$ in Figure 20 after MoO_3 deposition [45]. The sample was only exposed to air between these measurements, and the C1s peak after helium ion irradiation is again indicating C−C bonding. This might suggest that the sample have adsorbed some contaminants while being exposed to the atmosphere, which was then desorbed during the ion bombardment. However, as the sample was covered by the same amount of MoO_3 between deposition and irradiation, this explanation seems unlikely. Another explanation is that the shift is caused by experimental errors. As for the work function measurements in Table 5, they are significantly higher than the expected $\Phi \approx 6.6\,\mathrm{eV}$ before exposure ($\sim 2.3\,\mathrm{nm}$ MoO_3) and $\Phi \approx 5.8\,\mathrm{eV}$ after irradiation ($\sim 0.5\,\mathrm{nm}$ MoO_3) according to Russel *et al.* [12]. The reason for this is the same as discussed in section 6.1.2, namely that the origin of the photoelectrons is ambiguous. This is also the case for the ionization energy and electron affinity.

6.2 Improvements and Further Work

The analysis in section 6.1 poses several limitations in the experimental setup that should assessed in order to create a better foundation for interpretation of the results. There are also additional techniques that could be incorporated to get a more precise overview of the effects that are induced through exposure to radiation.

6.2.1 Photoemission Measurements

Due to the ambiguous results from PES, surface property characterization should be performed *before* the devices are made, i.e. on bare hydrogen-terminated and adsorbate covered samples. This is due to the fact that these measurements generate spectra based on entire regions, which makes it difficult to interpret the origin of the photoelectrons when measuring on devices with contacts and oxygen terminated regions. In addition, the work function of the detector should be accounted for in the XPS measurements to yield more accurate results.

6.2.2 4-point Measurements

Consecutive ex-situ 4-point measurements using probes will damage the contact pads and increase the risk of contamination. As a result, it is difficult to ensure the comparability of measurements due to possible bad contact points. For this reason, the contacts should be wire bonded to ensure high quality measurement contacts that yield reliable and comparable results. This would also allow for in-situ *I-V* measurements.

6.2.3 Contact Characterization

As previously stated, exposure to low-energy electrons causes ESD, and is therefore not ideal for this type of samples. It is thus questionable whether or not SEM should be used for investigation of the contact condition. For samples of this size, a simple optical microscope might provide sufficient information.

6.2.4 Electron Irradiation

A more precise solution for monitoring the dose rate should be incorporated. This may involve getting a reliable measure of the cross-sectional area of the beam or utilizing customized sensors. *I-V* measurements should be performed in-situ in order to see how the electrical characteristics change *during* exposure to electrons. This would give information about a possible critical dose where the conductivity suddenly drops, and provide a better overview of how electrons affect these devices. In addition, the effect of fluxes and energies comparable to that expected in space should be investigated in order to obtain a more comprehensive understanding of how this technology would respond to the environment.

6.2.5 Ion Irradiation

Dose monitoring and in-situ *I-V* measurements is also important for ion irradiation experiments. The effect of *proton* irradiation and higher energies should also be investigated. According to the theory in section 3.4, graphitization is dependent on dose rate, total dose and temperature. It would therefore be interesting to check experimentally how various combinations of these parameters affect the electrical properties.

6.2.6 Raman Analysis

The samples should ideally be smaller so that it would be possible to perform map scans with smaller steps between each spectrum, thus obtaining higher resolution maps. It would also be beneficial to perform 3-dimensional map scans using a confocal Raman in order to see the depth at which graphitization have occurred. This will provide information about whether or not graphitic regions could be responsible for changes in electrical behaviour. There are also several aspects of the data-analysis procedure that should be improved. Baseline corrections should be applied to the spectra to remove possible contributing fluorescence effects. In addition, noise reduction and removal should be incorporated to simplify data analysis and interpretation. Possible sample contamination may also have an effect on the result, so it is important to make sure that the sample is as clean as possible.

6.2.7 Surface Adsorbate

The *I-V* characteristics of the samples should be monitored in-situ during MoO_3 deposition in order to get a better idea whether or not the adsorbate itself is responsible for the decrease in conductivity. Some studies also suggest that vanadium pentoxide (V_2O_5) has a higher doping efficiency and stability compared to MoO_3 [46][13]. Using V_2O_5 as an alternative adsorbate for surface transfer doping should therefore be considered.

6.2.8 Uncertainties

Due to the lack of information about the uncertainties in the various parameters used in calculations for electrical and surface properties, a complete uncertainty analysis has not been performed. In order to do so, it is necessary to obtain information about uncertainties in the channel dimensions L and w for the electrical properties, as well as the uncertainties in the spectrometer output for the surface properties.

6.2.9 Correlation Between Common Materials

The effects of radiation on common semiconductor materials should be investigated and compared with that obtained for hydrogen terminated diamond with a comparable device geometry. This would be an important step towards fully understanding the circumstances under which diamond serves as a superior material for electronic devices.

7 Conclusion

The use of MoO_3 as an adsorbate for surface transfer doping of hydrogen terminated diamond did not result in an increased conductivity of the devices. In-situ *I-V* measurements should be used during deposition in the future in order to interpret the cause of this. Further, exposure to 3.5 keV electrons for $\sim$ 2 hours seem to have desorbed most of the deposited MoO_3 and possibly caused partly desorption of the hydrogen layer which resulted in a decrease in conductivity. The 5 keV helium ion exposure resulted in both decreased and increased conductivity for two separate devices on the same sample. This may indicate both desorption as well as formation of graphitic regions. In-situ *I-V* measurements and improved Raman analysis procedures should be incorporated to clarify the origin of these results. Apart from optimization of current measurement techniques, exposure to particles of higher energies should be considered in the future in order to get a better understanding of how this material would be affected by radiation in space.

8 References

[1] Z Li. Radiation Damage Effects in Si Materials and Detectors and Rad-hard Si Detectors for SLHC. *Journal of Instrumentation*, 4(03):P03011–P03011, mar 2009.

[2] Chris J.H. Wort and Richard S. Balmer. Diamond as an Electronic Material. *Materials Today*, 11(1-2):22–28, jan 2008.

[3] The Omere Software. `http://www.trad.fr/en/space/omere-software/`. Accessed: 2018-06-25.

[4] Helmuth Spieler. Introduction to Radiation-Resistant Semiconductor Devices and Circuits.

[5] Mark Thomas Edmonds. *Electronic properties of surface conducting hydrogen-terminated diamond*. PhD thesis, La Trobe University, 2013.

[6] J. B. Cui, J. Ristein, and L. Ley. Electron Affinity of the Bare and Hydrogen Covered Single Crystal Diamond (111) Surface. *Physical Review Letters*, 81(2), 1998.

[7] Antoine Kahn. Fermi Level, Work Function and Vacuum Level. *Materials Horizons*, 3(1):7–10, 2016.

[8] F. Maier, J. Ristein, and L. Ley. Electron Affinity of Plasma-Hydrogenated and Chemically Oxidized Diamond (100) Surfaces. *Physical Review B*, 64(165411), 2001.

[9] Golrokh Akhgar. Fabrication and Characterisation of Diamond Devices. Master's thesis, La Trobe University, 2014.

[10] F. Maier, M. Riedel, B. Mantel, J. Ristein, and L. Ley. Origin of Surface Conductivity in Diamond. *Physical Review Letters*, 85(16), 2000.

[11] M. Tordjman, C. Saguy, A. Bolker, and R. Kalish. Superior Surface Transfer Doping of Diamond with MoO_3. *Advanced Materials Interfaces*, 1(3), 2014.

[12] Stephen A. O. Russell, Liang Cao, Dongchen Qi, Alexandre Tallaire, Kevin G. Crawford, Andrew T. S. Wee, and David A. J. Moran. Surface transfer doping of diamond by MoO3: A combined spectroscopic and hall measurement study. *Applied Physics Letters*, 103(20):202112, nov 2013.

[13] C. Verona, W. Ciccognani, S. Colangeli, E. Limiti, Marco Marinelli, and G. Verona-Rinati. Comparative investigation of surface transfer doping of hydrogen terminated diamond by high electron affinity insulators. *Journal of Applied Physics*, 120(2):025104, jul 2016.

[14] W.Wang, C.Hu, F.N.Li, S.Y.Li, Z.C.Liu, F.Wang, J.Fu, and H.X.Wang. Palladium Ohmic Contact on Hydrogen-Terminated Single Crystal Diamond Film. *Diamond and Related Materials*, 59:90–94, 2015.

[15] *APPENDIX A HALL EFFECT MEASUREMENTS*. Lake Shore 7500/9500 Series Hall System User's Manual.

[16] H. Sumiya, N. Toda, and S. Satoh. Mechanical properties of synthetic type IIa diamond crystal. *Diamond and Related Materials*, 6(12):1841–1846, dec 1997.

[17] K. Tsugawa, A. Hokazono, Hiroshi Noda, K. Kitatani, Koichiro Morita, and Hiroshi Kawarada. MESFETs and MOSFETs on hydrogen-terminated diamond surfaces. *Materials Science Forum*, 264-268:977–980, feb 1998.

[18] Steve Appollo Yianni. *A Step-by-Step Process of a Device*. La Trobe University, Melbourne, Australia, 2017.

[19] Golrokh Akhgar, Daniel L. Creedon, Laurens H. Willems van Beveren, Alastair Stacey, David I. Hoxley, Jeffrey C. McCallum, Lothar Ley, Alex R. Hamilton, and Christopher I. Pakes. G-factor and well width variations for the two-dimensional hole gas in surface conducting diamond. *Applied Physics Letters*, 112(4):042102, jan 2018.

[20] Lucille A. Giannuzzi and Fred A. Stevie, editors. *Introduction to Focused Ion Beams*. Springer US, 2005.

[21] H. Shinotsuka, S. Tanuma, C. J. Powell, and D. R. Penn. Calculations of electron inelastic mean free paths. x. data for 41 elemental solids over the 50 eV to 200 keV range with the relativistic full penn algorithm. *Surface and Interface Analysis*, 47(12):1132–1132, oct 2015.

[22] S. Tanuma, C. J. Powell, and D. R. Penn. Calculations of Electron Inelastic Mean Free Paths. IX. Data for 41 Elemental Solids Over the 50 eV to 30 keV Range. *Surface and Interface Analysis*, 43(3):689–713, feb 2011.

[23] C. J. Powell and A. Jablonski. *NIST Electron Inelastic-Mean-Free-Path Database*, version 1.2 edition, 2010.

[24] Alex V. Hamza, Glenn D. Kubiak, and Richard H. Stulen. Hydrogen chemisorption and the structure of the diamond c(100)-(2 × 1) surface. *Surface Science*, 237(1-3):35–52, nov 1990.

[25] Hiraki A. Low-temperature cvd of diamond and nea surface of diamond. *Proceedings of the International School of Physics "Enrico Fermi"*, 135(The Physics of Diamond):179–193, 1997.

[26] R.D. Ramsier and J.T. Yates. Electron-Stimulated Desorption: Principles and Applications. *Surface Science Reports*, 12(6-8):246–378, jan 1991.

[27] James F. Ziegler, M.D. Ziegler, and J.P. Biersack. SRIM – The Stopping and Range of Ions in Matter (2010). *Nuclear Instruments and Methods in Physics Research Section B: Beam Interactions with Materials and Atoms*, 268(11-12):1818–1823, jun 2010.

[28] J.F. Ziegler and J.M. Manoyan. The stopping of ions in compounds. *Nuclear Instruments and Methods in Physics Research Section B: Beam Interactions with Materials and Atoms*, 35(3-4):215–228, dec 1988.

[29] M. Petravić and J.S. Williams. Electronic effects in ion-stimulated desorption of positive halogen ions from semiconductor surfaces. *Nuclear Instruments and Methods in Physics Research Section B: Beam Interactions with Materials and Atoms*, 101(1-2):64–68, jun 1995.

[30] R. Kalish and S. Prawer. Graphitization of Diamond by Ion Impact: Fundamentals and Applications. pages 492–499, 1996.

[31] S. Prawer and R. Kalish. Ion-beam-induced transformation of diamond. *Phys. Rev. B*, 51:15711–15722, Jun 1995.

[32] Scanning Electron Microscope. `https://en.wikipedia.org/wiki/Scanning_electron_microscope`. Accessed: 2017-11-01.

[33] Hitachi Hight-Tech. *Hitachi Tabletop Microscope TM3000*, 2011.

[34] Nanoprobing SEM Solutions. `http://www.imina.ch/products/Nanoprobing-SEM-Solution-Package#product-images`. Accessed: 2017-12-14.

[35] Akari Takayama. Basic principle of photoemission spectroscopy and spin detector. pages 15–30, sep 2014.

[36] A. BenMoussa, A. Soltani, U. Schühle, K. Haenen, Y.M. Chong, W.J. Zhang, R. Dahal, J.Y. Lin, H.X. Jiang, H.A. Barkad, B. BenMoussa, D. Bolsee, C. Hermans, U. Kroth, C. Laubis, V. Mortet, J.C. De Jaeger, B. Giordanengo, M. Richter, F. Scholze, and J.F. Hochedez. Recent Developments of Wide-Bandgap Semiconductor Based UV Sensors. *Diamond and Related Materials*, 18(5-8):860–864, may 2009.

[37] D. John O'Connor, Brett A. Sexton, and Roger St. C. Smart, editors. *Surface Analysis Methods in Materials Science*. Springer Berlin Heidelberg, 2003.

[38] M.G. Helander, M.T. Greiner, Z.B. Wang, and Z.H. Lu. Pitfalls in Measuring Work Function Using Photoelectron Spectroscopy. *Applied Surface Science*, 256(8):2602–2605, feb 2010.

[39] Herman A. Szymanski, editor. *Raman Spectroscopy*. Springer US, 1967.

[40] Joe Hodkiewicz. *Characterizing Carbon Materials With Raman Spectroscopy*. Thermo Fisher Scientific. Application Note: 51901.

[41] Vilde F. Rieker. Transistors for commercial space applications. Tfy4510 physics specialization project, Norwegian University of Science and Technology, 2018.

[42] Lili Cai, Connor J. McClellan, Ai Leen Koh, Hong Li, Eilam Yalon, Eric Pop, and Xiaolin Zheng. Rapid Flame Synthesis of Atomically Thin MoO3 down to Monolayer Thickness for Effective Hole Doping of WSe2. *Nano Letters*, 17(6):3854–3861, jun 2017.

[43] F. Rull, A. C. Prieto, J. M. Casado, F. Sobron, and H. G. M. Edwards. Estimation of Crystallinity in Polyethylene by Raman Spectroscopy. *Journal of Raman Spectroscopy*, 24(8):545–550, aug 1993.

[44] Jihye Bong, Kyuseok Choi, Soo-Chang Yu, Soo-Il Kwon, Yura Cho, Chaehee Park, and Hyung wook Park. Raman Spectroscopy of Irradiated Normoxic Polymethacrylic Acid Gel Dosimeter. *Journal of Raman Spectroscopy*, 32(2), feb 2011.

[45] Nguyen TK Thanh, editor. *Magnetic Nanoparticles: From Fabrication to Clinical Applications*. CRC Press, 2012.

[46] Kevin G. Crawford, Liang Cao, Dongchen Qi, Alexandre Tallaire, E. Limiti, C. Verona, Andrew T. S. Wee, and David A. J. Moran. Enhanced Surface Transfer Doping of Diamond by V2O5 with Improved Thermal Stability. *Applied Physics Letters*, 108(4):042103, jan 2016.

List of Abbreviations

2DHG Two-Dimensional Hole Gas. 6

COTS Commercial Off-The-Shelf. 1

DUT Device Under Test. 16

ESD Electron-Stimulated Desorption. 11

FET Field-Effect Transistor. 8

IMFP Inelastic Mean Free Path. 10

ISD Ion-Stimulated Desorption. 12

MOSFET Metal-Oxide-Semiconductor Field-Effect-Transistor. 2

NEA Negative Electron Affinity. 4

PEA Positive Electron Affinity. 4

PES Photoemission Spectroscopy. 16

S1D1 Sample 1 Device 1. 20

S2D1 Sample 2 Device 1. 21

SEM Scanning Electron Microscope. 14

SMU Source Measure Unit. 14

SRIM Stopping Range of Ions in Matter. 12

TRIM Transmission of Ions in Matter. 12

UHV Ultra-High Vacuum. 6

UPS Ultraviolet Photoemission Spectroscopy. 16

XPS X-Ray Photoemission Spectroscopy. 16

Nomenclature

χ	Electron affinity
Δw	Raman shift
$\dot{D}$	Dose rate
μ	Carrier mobility
μ_e	Chemical potential
Φ	Work function
ρ_H	Hall resistivity
ρ_s	Sheet resistivity
σ_0	Drude conductivity
D	Total dose
D_c	Critical dose
E_B	Binding energy
E_C	Conduction band minimum
E_F	Fermi level
E_G	Band gap
E_V	Valence band maximum
E_{VAC}	Vacuum level
I	Ionization energy
n_s	Sheet carrier density

Appendix A H-Diamond FET

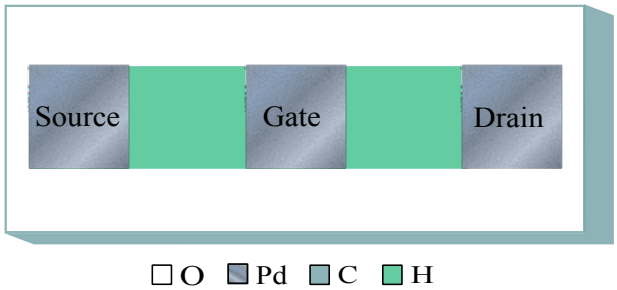

Figure 44: Geometry of a diamond FET. The current between the source and drain terminals are controlled by applying a potential at the gate.

Appendix B Raman Map-Analysis Script

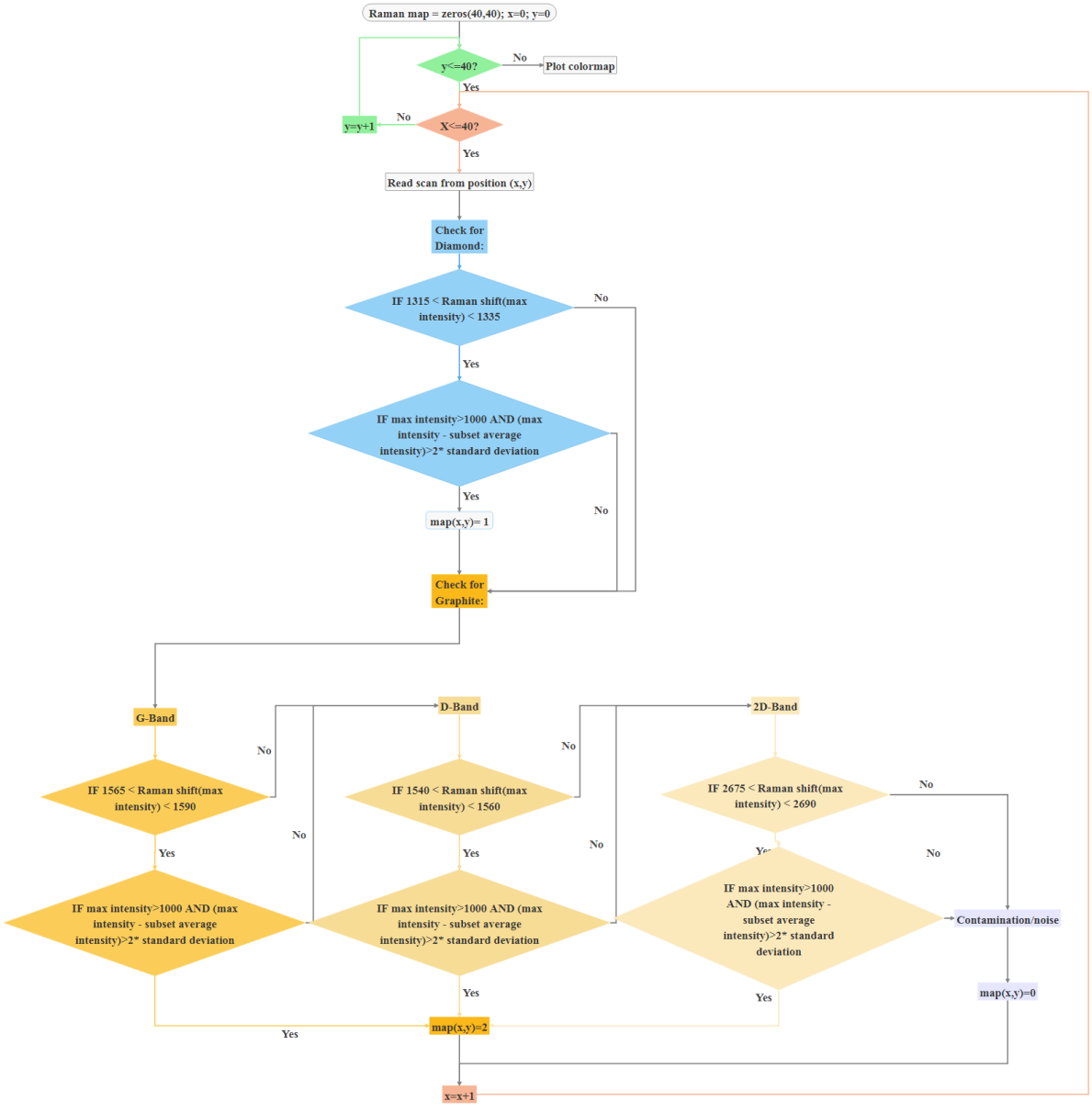

Figure 45: MATLAB script for Raman map-analysis.